nature materials

LETTERS

PUBLISHED ONLINE: 10 JULY 2011 | DOI: 10.1038/NMAT3069

Face-selective electrostatic control of hydrothermal zinc oxide nanowire synthesis

Jaebum Joo[1,2]*, Brian Y. Chow[1,3]*†, Manu Prakash[1,4]†, Edward S. Boyden[1,3] and Joseph M. Jacobson[1]

Rational control over the morphology and the functional properties of inorganic nanostructures has been a long-standing goal in the development of bottom-up device fabrication processes. We report that the geometry of hydrothermally grown zinc oxide nanowires[1–4] can be tuned from platelets to needles, covering more than three orders of magnitude in aspect ratio (~0.1–100). We introduce a classical thermodynamics-based model to explain the underlying growth inhibition mechanism by means of the competitive and face-selective electrostatic adsorption of non-zinc complex ions at alkaline conditions. The performance of these nanowires rivals that of vapour-phase-grown nanostructures[5,6], and their low-temperature synthesis (<60 °C) is favourable to the integration and *in situ* fabrication of complex and polymer-supported devices[7–9]. We illustrate this capability by fabricating an all-inorganic light-emitting diode in a polymeric microfluidic manifold. Our findings indicate that electrostatic interactions in aqueous crystal growth may be systematically manipulated to synthesize nanostructures and devices with enhanced structural control.

As a low-temperature aqueous process, hydrothermal synthesis[1–3,10–12] or crystallization from supersaturated aqueous solutions[3,10] holds great promise for nanostructure synthesis on a variety of substrates, and so far has been reported in the construction of several energy-harvesting and electronic devices[13,14]. The functions of these devices are critically linked to nanostructure morphology and hence require parameter tuning for optimal performance. Therefore, a predictive model-based hydrothermal synthesis that enables rational control over nanostructure morphology would greatly advance bottom-up nanoscience. To this end, many growth parameters have been previously explored to manipulate the morphology of hydrothermally synthesized ZnO nanowires[3,10], including the addition of auxiliary agents such as organic ligands and metal-ion impurities[2,4,12,14,15]. Previous findings that pH-dependent electrostatic interactions between zinc reactants and the crystal can influence the preferred growth direction[2,11,16,17] suggest that such interactions may provide a potential modality of control over ZnO nanowire morphology. Expanding on these explorations, a rational approach to systematically alter nanowire morphology bidirectionally (namely increasing or decreasing the aspect ratio) by means of electrostatics is developed here.

The primary principle underlying rational control during hydrothermal synthesis is face-selective electrostatic interaction. By introducing ancillary non-zinc sulphates into this reaction, we are able to systematically control the local reaction environment during the growth phase. The non-zinc ions form charged but largely unreactive complexes that can localize to the oppositely charged crystal surfaces, thereby competitively limiting the access of the reactive zinc intermediates and inhibiting growth in a crystal face-specific manner (Fig. 1). This mechanism is supported by the classical thermodynamic modelling provided here and validated by the ability to predict the effect of introducing various non-zinc ions on the aspect ratio of ZnO nanowires. The further understanding of electrostatics in controlled aqueous growth may enhance the syntheses of other inorganic structures, such as biomineralized and biomimetically crystallized nanostructures[18,19], or *in situ* grown layer-by-layer assemblies[20].

Single-crystalline nanowires were grown on substrates with zinc oxide seed layers in aqueous solutions of 10 mM zinc sulphate with 0.3 M ammonium chloride to improve zinc-ion solubility (pH = 11, 60 °C). These reagents and the alkaline reaction condition were chosen because speciation plots of the relative concentrations of intermediate metal hydroxide- and amine-complexes could be calculated from known constants (see Supplementary Figs S1–S3 for parametric optimization for specific conditions). These plots are shown in Fig. 2a,b for individual zinc complex ions and their intermediates, binned by charge, respectively (see Supplementary Fig. S2 for constants and supersaturation plots). At pH = 11, both positive and negative complex ions are present, and thus each species may interact with the crystal in a face-selective manner[2,11,16,17], because the negative (0002) top surface plane and positive ($10\bar{1}0$) sidewalls were found to be differentially charged (as measured by atomic force microscopy (Supplementary Fig. S6) and X-ray photoelectron spectroscopy (Supplementary Fig. S7)).

Whereas adjusting pH alone in a zinc-only system had modest impact on aspect ratio (<1.5-fold range; Supplementary Fig. S5), adding charged non-zinc complex ions induces pronounced changes in aspect ratio (Fig. 1a,b) by a face-selective crystal growth inhibition mechanism that could be leveraged to systematically control aspect ratio over a >1,000-fold range. For example, introducing a small amount of cadmium sulphate into the reaction mixture (<20% equivalent versus zinc) led to low aspect ratio platelets (0.1 height/diameter ratio), suggesting that the positively charged cadmium complexes (>99% positive at pH = 11, Fig. 2c) were electrostatically attracted to the negatively charged top (0002) face, thus inhibiting growth along the preferred *c* axis by limiting the access of Zn complexes. Conversely, introducing aluminium sulphate into the reaction had the opposite effect, leading to high aspect ratio structures (>100 height/diameter ratio) by the suppression of sidewall growth from the negatively charged Al complexes (Fig. 2d).

[1]Center for Bits and Atoms, The Media Laboratory, Massachusetts Institute of Technology, Cambridge, Massachusetts 02139, USA, [2]Department of Materials Science and Engineering, Massachusetts Institute of Technology, Cambridge, Massachusetts 02139, USA, [3]Department of Biological Engineering and Department of Brain and Cognitive Sciences, Massachusetts Institute of Technology, Cambridge, Massachusetts 02139, USA, [4]Harvard Society of Fellows, Harvard University, Cambridge, Massachusetts 02138, USA. †Present addresses: Department of Bioengineering, University of Pennsylvania, Philadelphia, Philadelphia 19104, USA (B.Y.C.); Department of Bioengineering, Stanford University, Stanford, California 94305, USA (M.P.).
*e-mail: jbjoo@alum.mit.edu; bchow@media.mit.edu.

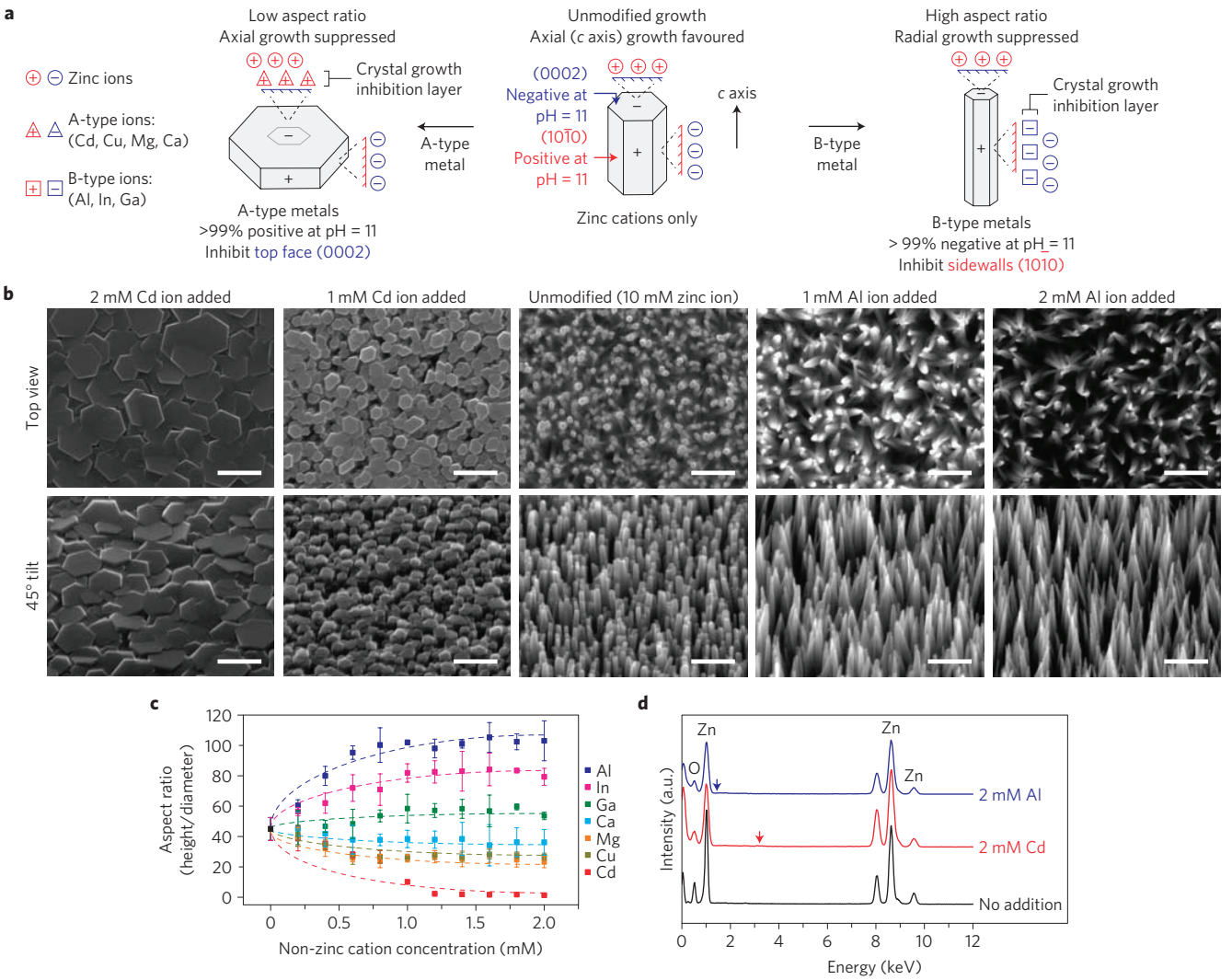

Figure 1 | Rational control over zinc oxide nanowire morphology by means of face-selective electrostatic crystal growth inhibition. a, Mechanism of control by non-zinc metal sulphates in the bath solution. A-type cations (positive at pH 11; Cd, Cu, Mg, and Ca) suppress axial growth at the negative (0002) face by limiting zinc complex-ion access, thus promoting platelet formation. Similar interactions between B-type ions (negative at pH 11; Al, In, Ga) and the positive (10$\bar{1}$0) sidewalls lead to high aspect ratio nanowires. **b**, Scanning electron micrographs of ZnO nanowires grown in the presence of Cd or Al. Scale bars = 500 nm. **c**, The aspect ratio was tunable over a >1,000-fold range (data point and error bars correspond to mean ± one standard deviation). Dotted trend lines are to guide the eye. **d**, Energy dispersive X-ray spectra of nanowires grown in the presence of 2 mM Al or Cd do not show readily observable Al (blue arrow, 1.49 keV) or Cd (red arrow, 3.13 keV) peaks.

Ancillary metal sulphates that formed predominately positively charged complex ions at pH = 11 were categorized as A-type (Cd, Cu, Mg, Ca), whereas ions that formed predominately negatively charged complexes were categorized as B-type (Al, In, Ga). The correlations between the aspect ratio and the relative charge distribution of complex ions, in which A-type and B-type ions promote low and high aspect ratio growth, respectively, were consistent for all sulphates tested (Fig. 1c and Supplementary Fig. S8), thus further supporting the model of face-selective electrostatic crystal growth inhibition (the presence of both metal ions was accounted for in all co-speciation plots, but typically led to <1% change in distributions). It is important to note that the tapered needle- or obelisk-like ends of high-aspect-ratio nanowires (resulting from the addition of B-type metals) were formed by multiple steps of hexagonal layers of growth with decreasing surface area[21], consistent with expected layer-by-layer growth mechanisms[21,22] (Supplementary Fig. S9). The taper does not represent the (10$\bar{1}$1) facets that are otherwise at 60° to the (0002) plane[23]. It should also be noted that factors beyond electrostatics may play a role, particularly at neutral pH, highly elevated temperature and/or extremely long reaction times (see Supplementary Information and Fig. S13). However, under the conditions reported here, the mechanism of bidirectional control over nanowire aspect ratio was dominated by electrostatics.

Given the low temperature, it was anticipated that non-zinc ions would have low incorporation rates into the growing ZnO crystal and, instead, their presence would primarily lead to crystal growth inhibition. Importantly, ZnO nanowires hydrothermally grown in the presence of non-zinc ions (2 mM, 20% equivalent versus zinc) did not seem to be significantly altered in their primary structure or optical properties, as confirmed by X-ray diffraction (Supplementary Fig. S10) and photoluminescence measurements (λ = 378 nm band-edge emission) (Supplementary Fig. S11). The energy-dispersive X-ray spectroscopy (EDS) plots for ZnO nanowires grown in the presence of cadmium or aluminium lack a readily observable 3.13 keV Cd peak or 1.49 keV Al peak (red and blue arrows in Fig. 1d, respectively). The findings above were consistent for all other ions tested. The limited

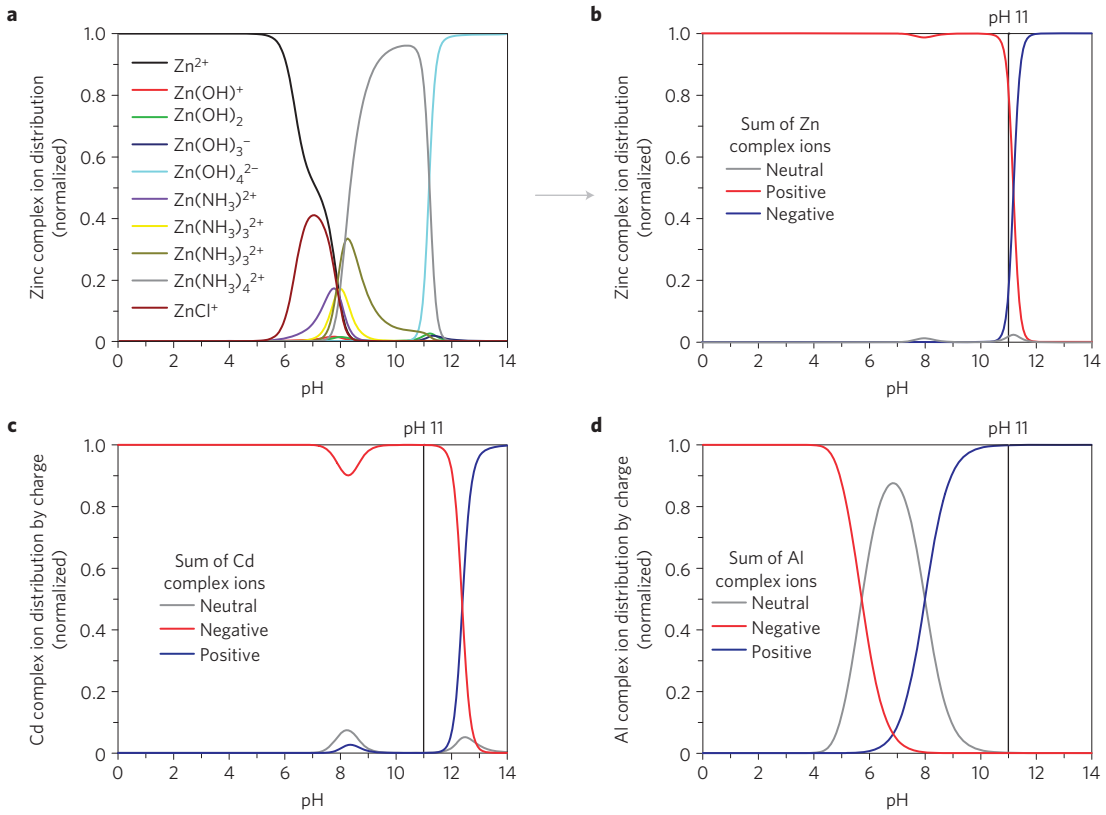

Figure 2 | Thermodynamic modelling of electrostatic interactions during hydrothermal synthesis. Relative concentrations of complex ion products formed from hydrolysis and aminolysis of metal sulphates were calculated from known reaction constants to derive pH-dependent speciation plots. **a**,**b**, Zinc complex ion distribution in a solution of 10 mM $ZnSO_4$ and 0.3 M NH_4Cl, normalized to the sum of the total ions, for individual species (**a**) and binned by charge (**b**). **c**,**d**, Speciation plots for Cd (**c**) and Al (**d**) complex ions binned by charge (also with 0.3 M NH_4Cl), as exemplar A- and B-type ions (see Fig. 1). Cd or Al complex ions are >99% positively or negatively charged at pH = 11, respectively. The model predicts face-selective crystal growth inhibition through the electrostatic adsorption of positive Cd complex ions at the negative (0002) plane, or of negative Al complex ions at the positive $(10\bar{1}0)$ plane.

incorporation or alteration of intrinsic material properties during the low-temperature aqueous synthesis differs from the more significant ion exchange or doping that occurs for high-temperature aqueous reactions driven in pressurized autoclaves[2,24], at high temperature in organic solvents[25] or during co-introduction of gases in vapour–liquid solid (VLS) synthesis[6].

As a result of the large formation enthalpy required for non-zinc ions to be incorporated into the ZnO crystal, the estimated maximum solubility or doping achievable under the conditions here is $\sim 10^{-5}$ (see Supplementary Information). Given this low solubility, the electrostatically adsorbed ancillary complexes mainly blocked the available crystal surface sites to inhibit Zn-complex binding. However, limited incorporation is expected on the basis of the estimated solubility and modest increase/decrease in defect emission (Supplementary Fig. S11), and the doping is more readily observed at much higher temperature and pressure[2,24] (for example, increased estimated maximum solubility by $\sim 10^2$ at 300 °C and $>10^8$ Pa). Thus, the ability to use inorganic ions largely as surface-binding ligand-like complexes highlights the importance of maintaining low synthesis temperatures for morphology control.

The material compatibility and potential low-cost nature (including resource consumption) of the low-temperature aqueous synthesis were underlying motivations for developing systematic control mechanisms towards the enhancement of geometry-coupled properties and manufacturing of polymer-supported devices. Accordingly, we demonstrate greatly improved field emission from ZnO nanowires formed in the presence of aluminium ions, then create polymer-supported flexible a.c. electroluminescent devices with improved luminance efficiency, and construct a multilayer optoelectronic device completely *in situ* within a polymeric microreactor.

As the field emission of a nanoneedle scales as $\sim d/r$ (where d is nanowire length and r is the apex radius) accelerating to the Fowler–Nordheim equations[26], we exploit the above synthesized nanostructures as a field-emission source. Field emission of ZnO nanowires was greatly enhanced by the addition of aluminium sulphate into the growth solution (Fig. 3a), with turn-on field values (to reach 10 μA cm^{-2}) improved by a factor of >8 over nanowire emitters grown under unmodified conditions (0.45 V μm^{-1} with 2 mM Al versus 3.70 V μm^{-1} without). Conversely, field emission was inhibited by the addition of cadmium. The calculated field enhancement factor $\beta = 2.83 \times 10^4$ for nanowires grown in the presence of 2 mM aluminium sulphate (aspect ratio = 103) versus $\beta = 2.08 \times 10^3$ without modifiers was a near 14-fold improvement (Supplementary Fig. S14). These values for turn-on and enhancement rival those reported for VLS-synthesized carbon nanotube emitters (turn-on ~ 0.8 V μm^{-1}, β = 1,000–35,000; ref. 27), despite the very low temperature synthesis (<60 °C) that is favourable to device integration and *in situ* fabrication of polymer-supported nanodevices.

The combination of low-temperature processing in an aqueous environment and enhanced field emission is ideal for the fabrication of polymer-based, nanowire-embedded a.c. electroluminescent devices (NW-ACEL) (Fig. 3b–e). In a typical ACEL device, accelerated electrons from the emitter excite dopant atoms in a phosphor, leading to photon emission on atom relaxation to the

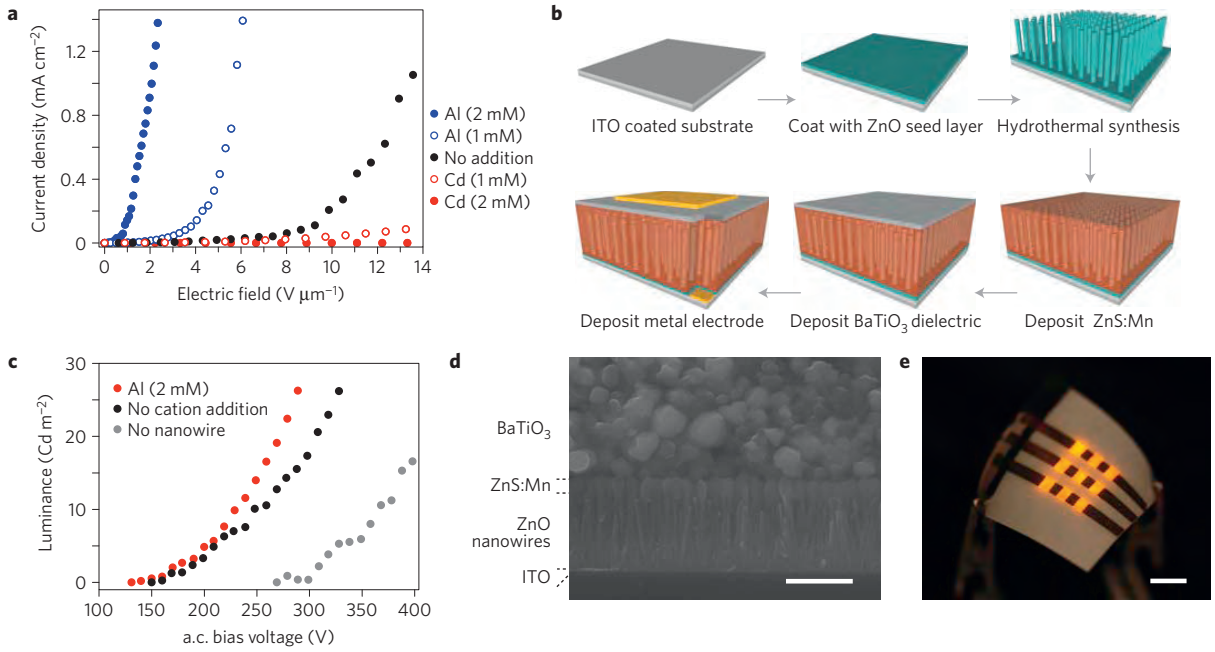

Figure 3 | Morphology-coupled field emission of ZnO nanowires for nanowire-embedded a.c. electroluminescent devices (NW-ACEL). a, Field emission of nanowires grown in the presence of Al (blue), no additional non-zinc ions (black), or Cd (red). Nanoneedles formed in the presence of 2 mM aluminium sulphate had similar emissivity to single-walled carbon nanotubes, despite the low-temperature synthesis (<60 °C). **b**, Process flow for a NW-ACEL device, where ZnO nanowires enhance field emission to the phosphor from the dielectric. **c**, The luminance and efficiency (Supplementary Table S2) of the ACEL device are improved by incorporating the NW-field enhancement layer (black), particularly by high aspect ratio nanoneedles (red). **d**, Cross-sectional scanning electron micrographs of the device. Scale bar = 1 μm. **e**, NW-ACEL device fabricated on flexible polyethylene terephthalate (PET). The device was operated at 260 V_{rms} at 5 kHz. Scale bar = 5 mm.

ground state. ACEL devices typically have poor efficiency, and thus to improve performance, a NW-ACEL device—with nanoneedles embedded into a ZnS:Mn phosphor layer to enhance field emission from the dielectric ZnO seed layer—was fabricated on flexible, metal-coated polyethylene terepthalate (PET). The yellow/orange electroluminescence spectrum matched the photoluminescence spectrum of the phosphor (Supplementary Fig. S15), indicating that the nanoneedles acted as a field-enhancement layer, as opposed to directly emitting by electron–hole recombination within the semiconductor. The voltage-dependent luminance curves (Fig. 3c) show that the enhancement layer lowers the turn-on voltage by a factor of typically 1.5–2 per luminance unit, and improves maximum luminance efficiency by an order of magnitude (Supplementary Table S2).

Furthermore, polymer-compatible low-temperature *in situ* syntheses give possibilities beyond integration onto plastics, such as synthesis in elastomeric microfluidic environments[7,28]. When nanowires were synthesized in a continuous flow polydimethylsiloxane microreactor, the addition of cadmium and aluminium ions had the same effect on morphology change as in the batch synthesis process (Supplementary Figs S16 and S17). Synthesis rates were five times higher in the microfluidic device than in bulk solution because of the constant replenishing of reagents and clearance of homogenous nucleants that consume reactants in solution. Aspect ratios of the structures were effectively unchanged by growth in the microfluidic environment, which supports the notion of improved mass transport being dominant. The nanowire vertical growth rate in the microfluidic device was typically 1.5–2 μm h^{-1} versus 0.3–0.4 μm h^{-1} in the optimized batch reactor.

Beyond improved mass transport, hydrothermal synthesis in a microfluidic environment enables parallel screening of synthesis parameters with minimal reagent consumption (Supplementary Fig. S17). Microfluidics-based, surface-adherent synthesis also offers a route towards simultaneous spatial patterning of functional materials[9,29,30]. As an example, we demonstrate an all-inorganic *in situ* fabricated multi-layer light-emitting diode, by sequentially flowing solution-processable reagents (Fig. 4). Here, the microfluidic manifold acts not only as a micro-reactor that improves the control over synthesis parameters and vastly diminishes reagent consumption, but also as the bottom-up fabrication house of a multilayer opto-electronic device, and finally, as the packaged end-device itself. The self-aligned *in situ* synthesis and integration into a functional device eliminates the transfer printing or etching steps typically involved in flexible electronics.

The metal–insulator–semiconductor light emitting diode (M–I–S LED) was *in situ* fabricated by sequentially synthesizing nanowires in a microfluidic manifold on top of indium tin oxide (ITO)-coated glass or PET, and subsequently flowing in an insulating spin-on-glass through the channel, followed by a low-melting solder that fills the remainder of the channel[8] (Fig. 4a,b). The device had an apparent 4 V turn-on voltage and a 10^{-8} A reverse current (or 5×10^{-6} A cm^{-2} current density, Supplementary Fig. S18), both indicative of diode function. The fully fabricated and packaged device is optically transparent, as shown in the top inset of Fig. 4c, and light emission from an individually addressed pixel in the ON and OFF states is shown in the lower insets (Fig. 4c). The ability to completely *in situ* fabricate a multi-layer all-inorganic device with minimal reagent consumption highlights the importance of low-temperature hydrothermal synthesis and improved mechanisms for systematic control.

The chemical system presented here provides a framework for an understanding of pH-dependent surface interactions in complex reaction mixtures, on which one can build further understanding. Our model-based experiments established electrostatics as a dominant control mechanism in low-temperature alkaline hydrothermal synthesis, and further demonstrated the efficient creation of ZnO nanowire-based devices with enhanced properties and critical features for manufacturing nanostructure-based devices

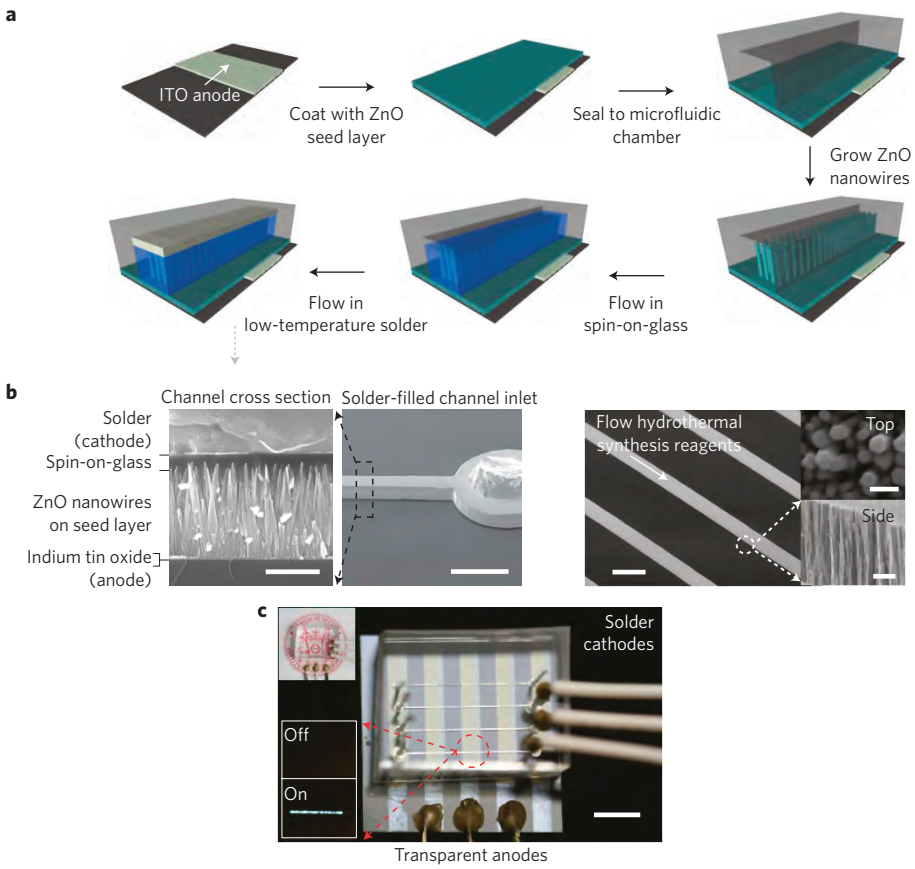

Figure 4 | *In situ* fabrication of an all-inorganic multi-layer opto-electronic device in a microfluidic manifold. a, Process flow for the *in situ* fabrication of a metal–insulator–semiconductor light-emitting diode (M–I–S LED). The polymeric manifold serves as a micro-reactor, bottom-up fabrication house, and the packaged end-device itself. **b**, Scanning electron microscopy characterization of the device. Left panels: Cross-section of the complete device. Scale bars = 500 nm (left), 500 μm (right). Right panels: Nanowires grown in the microfluidic environment exhibit conformal sidewalls and a fivefold increased growth rate (over batch synthesis). Scale bars = 200 μm (left), 500 μm (top right), 2 μm (bottom right). **c**, Transparent M–I–S LED imaged at a slight angle to enhance feature contrast. Top inset depicts transparency of the device at a perpendicular view point. Bottom inset shows emission in the on- and off-states at a forward bias of 10 V. Scale bar = 5 mm.

with respect to cost, material integration compatibility, and resource consumption. The synthesis is amenable to processing in microfluidic reactors, yielding multi-layer *in situ* synthesis paradigms for spatially complex functional devices. Thus, the development of an electrostatic mechanism to systematically manipulate nanowire aspect ratio may further nanomaterials synthesis chemistry towards the goal of rational control over nanostructure morphology.

Methods

Single-crystalline nanowires were grown on substrates with zinc oxide seed layers (deposited by sputtering or spin-coating of sol–gels), in aqueous solutions of 10 mM zinc sulphate and 0.3 M ammonium chloride at pH = 11, 50–60 °C. Non-zinc metal sulphates were added to the solution before growth. All reagents were used as received from Sigma-Aldrich unless noted otherwise; deionized water was 18.2 MΩ Millipore water. Alternating current electroluminescent devices were fabricated by first RF sputtering 30 nm-thick seed layers on top of patterned electrodes (by wet-etching of indium tin oxide-coated substrates with aqueous $FeCl_3$/HCl or thermal evaporation of thin gold films), synthesizing nanowires to a thickness of 1.2 μm (in the presence of 2 mM aluminium sulphate), RF sputtering of ZnS:Mn phosphor (K. J. Lesker), spin-coating of 13 μm-thick barium titanate paste as dielectric (Dupont LuxPrint 8153), and deposition of a conductive electrode. Microfluidic devices were fabricated by standard processes, using polydimethylsiloxane (PDMS, Sylgard 184) cast off of molds composed of SU-8 photoresist (Microchem) on silicon wafers, patterned by standard lithographic techniques. The temperature within the microfluidic manifold was controlled by means of a Peltier stage. The M–I–S LED was *in situ* fabricated by sequentially synthesizing nanowires in a microfluidic manifold on top of ITO-coated glass or PET (50 °C for 30 min at flow rate = 0.6 ml h^{-1}), flowing in a spin-on-glass through the channel to a film thickness of 240 nm (200 °C for 10 s at flow rate = 1 ml h^{-1}), followed by a low-melting solder that fills the remainder of the channel (In52/Sn48 from AIM Specialty) at 200 °C with low vacuum applied at the fluid outlet[8]. Thermodynamic calculations were performed in MATLAB. Spectroscopy and metrology were performed with the following: scanning electron microscopy (FEI XL30), atomic force microscopy (Digital Instruments Dimension 3000), transmission electron microscopy (JEOL 2010 with an EDS unit), X-ray diffractometry (PANalytical X'Pert PRO), photoluminescence (Hitachi F7000), X-ray photoelectron spectroscopy (PHI 5701 LSci), electroluminescence spectroscopy (Ocean Optics HR2000), photoluminescent spectroscopy (Nanolog fluorescence spectrometer, Horiba Jovin Yvon), luminance measurements (Konica Minolta CS-200), and solid-state device testing (custom built micromanipulator with Keithley 237 high-voltage analyzer). During scanning electron microscopy analysis, the diameter was measured at the midpoint along the *c*-axis of the nanowire.

Received 1 November 2010; accepted 9 June 2011; published online 10 July 2011

References

1. Vayssieres, L. Growth of arrayed nanorods and nanowires of ZnO from aqueous solutions. *Adv. Mater.* **15,** 464–466 (2003).
2. Demianets, L. N., Kostomarov, D. V., Kuz'mina, I. P. & Pushko, S. V. Mechanism of growth of ZnO single crystals from hydrothermal alkali solutions. *Crystallogr. Rep.* **47,** S86–S98 (2002).
3. Govender, K., Boyle, D. S., Kenway, P. B. & O'Brien, P. Understanding the factors that govern the deposition and morphology of thin films of ZnO from aqueous solution. *J. Mater. Chem.* **14,** 2575–2591 (2004).
4. Tian, Z. R. R. *et al.* Complex and oriented ZnO nanostructures. *Nature Mater.* **2,** 821–826 (2003).

5. Wagner, R. S. & Ellis, W. C. Vapor–liquid–solid mechanism of single crystal growth. *Appl. Phys. Lett.* **4,** 89–90 (1964).
6. Morales, A. M. & Lieber, C. M. A laser ablation method for the synthesis of crystalline semiconductor nanowires. *Science* **279,** 208–211 (1998).
7. Song, Y. J., Hormes, J. & Kumar, C. Microfluidic synthesis of nanomaterials. *Small* **4,** 698–711 (2008).
8. Siegel, A. C., Bruzewicz, D. A., Weibel, D. B. & Whitesides, G. M. Microsolidics: Fabrication of three-dimensional metallic microstructures in poly(dimethylsiloxane). *Adv. Mater.* **19,** 727–733 (2007).
9. Lee, S. H. *et al.* Control of the ZnO nanowires nucleation site using microfluidic channels. *J. Phys. Chem. B* **110,** 3856–3859 (2006).
10. Lincot, D. Solution growth of functional zinc oxide films and nanostructures. *MRS Bull.* **35,** 778–789 (2010).
11. Richardson, J. J. & Lange, F. F. Controlling low temperature aqueous synthesis of ZnO. 1. Thermodynamic analysis. *Cryst. Growth Des.* **9,** 2570–2575 (2009).
12. Greene, L. E., Yuhas, B. D., Law, M., Zitoun, D. & Yang, P. D. Solution-grown zinc oxide nanowires. *Inorg. Chem.* **45,** 7535–7543 (2006).
13. Ju, S. *et al.* Fabrication of fully transparent nanowire transistors for transparent and flexible electronics. *Nature Nanotech.* **2,** 378–384 (2007).
14. Law, M., Greene, L. E., Johnson, J. C., Saykally, R. & Yang, P. D. Nanowire dye-sensitized solar cells. *Nature Mater.* **4,** 455–459 (2005).
15. Zhang, R. & Kerr, L. L. A simple method for systematically controlling ZnO crystal size and growth orientation. *J. Solid State Chem.* **180,** 988–994 (2007).
16. Demianets, L. N. & Kostomarov, D. V. Mechanism of zinc oxide single crystal growth under hydrothermal conditions. *Ann. Chim. Sci. Mater.* **26,** 193–198 (2001).
17. Belghiti, H. E., Pauporté, T. & Lincot, D. Mechanistic study of ZnO nanorod array electrodeposition. *Phys. Status Solidi A* **205,** 2360–2364 (2008).
18. Kisailus, D., Schwenzer, B., Gomm, J., Weaver, J. C. & Morse, D. E. Kinetically controlled catalytic formation of zinc oxide thin films at low temperature. *J. Am. Chem. Soc.* **128,** 10276–10280 (2006).
19. Cha, J. N. *et al.* Silicatein filaments and subunits from a marine sponge direct the polymerization of silica and silicones *in vitro*. *Proc. Natl Acad. Sci. USA* **96,** 361–365 (1999).
20. Hammond, P. T. Recent explorations in electrostatic multilayer thin film assembly. *Curr. Opin. Colloid Interface Sci.* **4,** 430–442 (1999).
21. Laudise, R. A., Kolb, E. D. & Caporaso, A. J. Hydrothermal growth of large sound crystals of zinc oxide. *J. Am. Ceram. Soc.* **47,** 9–12 (1964).
22. Morin, S. A., Bierman, M. J., Tong, J. & Jin, S. Mechanism and kinetics of spontaneous nanotube growth driven by screw dislocations. *Science* **328,** 476–480 (2010).
23. Li, W. J., Shi, E. W., Zhong, W. Z. & Yin, Z. W. Growth mechanism and growth habit of oxide crystals. *J. Cryst. Growth* **203,** 186–196 (1999).
24. Dem'yanets, L. N., Kostomarov, D. V. & Kuz'mina, I. P. Chemistry and kinetics of ZnO growth from alkaline hydrothermal solutions. *Inorg. Mater.* **38,** 124–131 (2002).
25. Son, D. H., Hughes, S. M., Yin, Y. D. & Alivisatos, A. P. Cation exchange reactions in ionic nanocrystals. *Science* **306,** 1009–1012 (2004).
26. Fowler, R. H. & Nordheim, L. Electron emission in intense electric fields. *Proc. R. Soc. Lond. A* **119,** 173–181 (1928).
27. Jo, S. H. *et al.* Field emission of carbon nanotubes grown on carbon cloth. *J. Vac. Sci. Technol. B* **23,** 2363–2368 (2005).
28. Chan, E. M., Mathies, R. A. & Alivisatos, A. P. Size-controlled growth of CdSe nanocrystals in microfluidic reactors. *Nano Lett.* **3,** 199–201 (2003).
29. Wu, Y. *et al.* Inorganic semiconductor nanowires: Rational growth, assembly, and novel properties. *Chem. Eur. J.* **8,** 1260–1268 (2002).
30. Wang, J. *et al.* Electrochemical fabrication of conducting polymer nanowires in an integrated microfluidic system. *Chem. Commun.* 3075–3077 (2006).

Acknowledgements

This research was funded by the Center for Bits and Atoms (NSF CCR0122419) and the MIT Media Lab. We thank S. Manalis, V. Bulovic, and A. Belcher for generously providing use of equipment. The authors acknowledge the partial support of the Korea Foundation for Advanced Studies (awarded to J.J.) and Samsung (research internship to J.J.); the Harvard Society of Fellows (awarded to M.P.); and the Wallace H. Coulter Early Career Award, NARSAD Young Investigator Award, NSF, and NIH Director's New Innovator Award (awarded to E.S.B.).

Author contributions

J.J. and B.Y.C. designed all the experiments. J.J. conducted all the experiments. B.Y.C. assisted with device fabrication, microfluidics, and spectroscopy. M.P. assisted with microfluidics. All authors contributed to data analysis and writing of the manuscript.

Additional information

The authors declare no competing financial interests. Supplementary information accompanies this paper on www.nature.com/naturematerials. Reprints and permissions information is available online at http://www.nature.com/reprints. Correspondence and requests for materials should be addressed to J.J. or B.Y.C.

nature materials

SUPPLEMENTARY INFORMATION

DOI: 10.1038/NMAT3069

Face-selective electrostatic control of hydrothermal zinc oxide nanowire synthesis

Jaebum Joo[1,2(*)], Brian Y. Chow[1,3,5], Manu Prakash[1,4,6], Edward S. Boyden[1,3], and Joseph M. Jacobson[1]

[1] Center for Bits and Atoms, The Media Laboratory, Massachusetts Institute of Technology, Cambridge, MA 02139. [2] Dept. of Materials Science and Engineering, Massachusetts Institute of Technology, Cambridge, MA 02139. [3] Dept. of Biological Engineering and Dept. of Brain and Cognitive Sciences, Massachusetts Institute of Technology, Cambridge, MA 02139. [4] Harvard Society of Fellows, Harvard University, Cambridge, MA 02138. [5] Current location: Dept. of Bioengineering, University of Pennsylvania, Philadelphia, PA 19104. [6] Current location: Dept. of Bioengineering, Stanford University, Stanford, CA 94305

(*) Correspondence: jbjoo@alum.mit.edu

I. Materials and Methods

All reagents were used as received from Sigma-Aldrich unless noted otherwise. Water was 18.2 MΩ Millipore water. Calculations were performed in MATLAB.

I.A. *Nanowire synthesis*

A pre-cleaned substrate (silicon, glass or flexible polyethylene therephthalate, PET) was coated with a zinc oxide seed layer (ZnO, 2 – 30nm thick) by either RF sputtering (150W, 20mTorr, 12sccm Ar) or sol-gel spin coating (0.7M zinc acetate dihydrate and 0.7M monoethanolamine in 2-Methoxyethanol, 3000 rpm for 40 sec, followed by curing for 10 minutes on a 250°C hotplate). The substrate was placed upside down in a 100 mL solution in a closed jar containing zinc sulfate and ammonium chloride, pH adjusted with sodium hydroxide (~125mM final concentration sodium). Unless stated otherwise, syntheses were performed at 60°C by placing the jar in a convection oven, with a solution composition of 10 mM zinc sulfate and 300 mM ammonium chloride at pH = 11. Ancillary metal sulfate hydrates (≤ 2 mM Al, In, Ga, Ca, Mg, Cu, or Cd) were added to such a solution before pH adjustment. The concentrations of these modifiers were limited to avoid modifier oxide precipitation.

I.B. *Device Fabrication*

I.B1. *Nanowire Alternative Current Electroluminescent Device (NW-ACEL)*

Pre-cleaned (solvent washes by acetone, isopropanol, deionized water, and dried under nitrogen) indium tin oxide-coated glass (ITO glass, Delta Technologies) was patterned by standard contact

DOI: 10.1038/NMAT3069

lithography procedures to form transparent and independently addressable electrodes: (1) spin coat AZ 4620 photoresist at 1500 rpm for 40sec, (2) prebaked at 90°C for 1hr, (3) exposed with 50mW/cm^2 i-line irradiation for 20sec (INTELLI-RAY 400, Uvitron), (4) developed with AZ 440K developer, and then (5) wet chemical etching with ferric chloride (FeCl3, 25~30%) mixed with hydrochloric acid (HCl, 1~5%) in water for 2 hrs at room temperature, then cleaned with DI water. 30 nm-thick ZnO seed layers were deposited by RF sputtering. For flexible devices, 30 nm-thick Au films were thermally evaporated on PET (McMaster Carr) through a shadow mask (custom made with an Omax Waterjet) to create semi-transparent electrodes.

Nanostructures were synthesized to 1.2 μm film thickness (time to reach thickness by SEM: no additional ions - 4hr, 2mM Al - 6hr, 2mM Cd - 20hr), then removed from the bath, washed with water, and dried under nitrogen. 300 nm-thick ZnS:Mn phosphor layers were deposited over the nanostructures by RF sputtering (110W, 3mTorr, 12sccm Ar; 0.8 atomic % Mn target, Kurt J. Lesker) at 250°C on glass or 60°C on PET. Barium titanate paste (Dupont, LuxPrint 8153) was used to deposit 13 μm-thick dielectrics by spin coating at 4000 rpm for 50 seconds, followed by annealing at 150°C for 20 minutes. The top electrode was either deposited with Al by RF sputtering or brush painted using graphite paste (Ted Pella).

I.B2. *Microfluidic Nanowire Synthesis / In-Situ fabricated Metal-Insulator-Semiconductor LED*

Polydimethylsiloxane (PDMS, Dow Corning Sylgard 184) microfluidics were cast on molds composed of SU8 photoresist (Microchem) on silicon wafers, based on previously reported lithographic techniques [1-2]. For general synthesis and screening of reaction conditions in microfluidic devices, molded fluidic channels were attached to zinc oxide seed layer-coated substrates by compression sealing. Nanostructures were synthesized with this device placed on top of a Peltier stage (FerroTec) to modulate temperature.

For the metal-insulator-semiconductor light-emitting diode (MIS LED), a 0.1 mm x 0.08 x 15 mm (width x height x length) channel was bonded to a patterned ITO glass substrate coated with a ZnO seed layer via a “stamp and stick” method. Uncured PDMS pre-polymer (GE, RTV 615) at a component A to B ratio of 10 : 1 was spin-coat on top of a silicon wafer at 6000 rpm for 4 minutes. The molded channel was placed on top of the wafer to transfer the thin adhesion layer, and then it was placed on top of the ZnO-coated substrate, followed by curing in a convection oven at 80°C for 3 hours. Nanowire growth in the microfluidic channel was performed with same solution as described above, at 50°C (on top of a Peltier) for 30 minutes and at a flow rate of 0.6 mL/h. Spin-on-glass (SOG) was flown through the channel at a rate of 1 mL/h for 10 seconds at 200°C. The conformal top electrode was formed by flowing molten metal (In52 / Sn48, AIM Specialty Inc.) with a low vacuum from the opposite end of the channel at 200°C [3].

I.C. *Characterization*

The composition of the nanowires was characterized using a JEOL 2010F field emission transmission electron microscope (FE-TEM) equipped with an energy dispersive X-ray spectroscopy (EDS) unit. The morphology and aspect ratio of nanowires were measured using a FEI XL30 environmental scanning electron microscope (SEM), operated in normal high vacuum mode. Crystalline structure and orientation of the nanowires was identified by X-ray diffractometry (XRD, Panalytical X'pert Pro) using CuKα (1.5406Å) radiation. Photoluminescence of ZnO nanowires was measured with a spectrophotometer at room temperature (F7000, Hitachi; λ = 325nm from monochromatized Xe source).

Force-distance measurements were used to evaluate the surface potential of single crystalline ZnO surfaces. Au-coated contact mode AFM cantilevers (Budget Sensors, 0.2N/m) were chemically modified with carboxyl-terminated alkanethiol monolayers to ensure the cantilever was negatively charged under the testing conditions. Single crystal ZnO (MTI Corporation) with (0002), (10$\bar{1}$0), and (11$\bar{2}$0) planes were used. All crystals were thoroughly rinsed with DI water and dried under nitrogen. To measure surface potential of ZnO planes at pH 11, sodium hydroxide was used to adjust the pH of 1 mM aqueous KCl. The crystal was allowed to equilibrate for 5 minutes in solution prior to force-distance measurements taken at scan rate of 1 Hz (Digital Instruments Dimension 3000).

X-ray photoelectron spectroscopy (XPS) was used to determine the relative surface acidities of ZnO crystals with different orientations. ZnO crystals were coated with 5Å thick palladium (Pd) by RF sputtering (70W, 30mTorr, 12 sccm Ar). All XPS measurements were performed using monochromatic Al Kα radiation under ultra high vacuum (1.2 ~ 5 x 10^{-10} Torr) at a takeoff angle of 30^{o} from the plane. Pd 3d photoelectron peaks and Pd MMV auger peaks were measured to determine the modified auger parameter (MAP) of Pd as a function of crystalline orientation.

Field emission I-V characteristics were measured with nanostructures grown on ITO coated glass. A counter electrode was composed of tungsten (1.98 mm^2 area), and the spacing was fixed to 30 µm using a micromanipulator, for I-V characterization with a Keithley 237 high voltage analyzer under vacuum (10^{-5} mbar).

Photoluminescent spectra of ZnS:Mn were measured with a fluorescence spectrophotometer (Nanolog, Horiba Jovin Yvon) equipped with a 160 mW 488 nm Ar-ion laser (Spectra Physics) as an excitation source. Electroluminescent spectra of the nanowire ACEL device were measured with a fiber optic spectrometer (HR2000, Ocean Optics). Voltage dependent measurements were performed with a 5 kHz function generator (HP 33120A) and a high voltage amplifier (Trek). Luminance was measured using a Konica-Minolta CS-200 luminance color meter. The input power to the ACEL device was calculated by measuring the voltage drop across the device and a series resistor, and the phase angle between two signals with a Textronix 3054B oscilloscope.

DOI: 10.1038/NMAT3069

II. Supersaturation and growth of ZnO in chemical solution

Supersaturation levels are indicators of the driving force for hydrothermal growth. In the case of excessive driving forces, homogeneous nucleation and growth are enhanced, and ZnO nanostructures primarily form in solution instead of desired heterogeneous growth at the interface of the ZnO seed layer. Fig S1b shows this behavior under a poorly optimized condition (90°C), forming a turbid solution containing high levels of homogeneous nucleants and growth products.

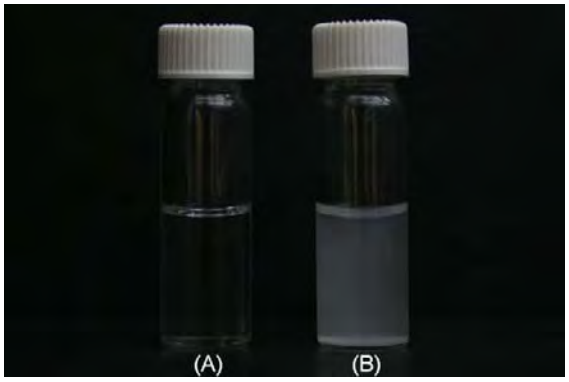

Fig. S1. 4mL aliquot of ZnO nanowire growth solutions after 30 minutes at **(A)** 60 °C and **(B)** 90°C, with the same solution composition ($ZnSO_4$ 10mM, NH_4Cl 0.3M, pH 11). The cloudy solution formed at elevated temperature results from homogenous nucleant-formation in bulk solution as opposed to the desired reagent consumption via heterogeneous nucleation resulting in nanowire growth on the substrate.

Figure S2 shows solubility plots calculated from the possible chemical reactions in a solution containing $ZnSO_4$, NH_4Cl, and NaOH. The x, y, and z axes indicate pH (NaOH dependent), NH_4Cl concentration, and maximum concentration of zinc ions without forming ZnO, respectively. For solutions with composition below the 3D contour plane shown in Figure S1b, no precipitation or nanowire growth will occur; nanowires will grow if the solution composition is above the plane of the 3D contour plot because the solution is supersaturated.

Similarly, solubility plots for the non-zinc metal/metal oxide (Cd, Al, Mg, and others) can be generated using relevant chemical reaction constants. Figure S2c shows one such example, for Cd.

(a)

Chemical Reaction	Log K
$Zn^{2+} + OH^- \leftrightarrow Zn(OH)^+$	5.0
$Zn^{2+} + 2OH^- \leftrightarrow Zn(OH)_2\ (aq)$	11.1
$Zn^{2+} + 3OH^- \leftrightarrow Zn(OH)_3^-$	13.7
$Zn^{2+} + 4OH^- \leftrightarrow Zn(OH)_4^{2-}$	18
$Zn^{2+} + NH_3 \leftrightarrow Zn(NH_3)^{2+}$	2.21
$Zn^{2+} + 2NH_3 \leftrightarrow Zn(NH_3)_2^{2+}$	4.5
$Zn^{2+} + 3NH_3 \leftrightarrow Zn(NH_3)_3^{2+}$	6.86
$Zn^{2+} + 4NH_3 \leftrightarrow Zn(NH_3)_4^{2+}$	8.89
$Zn^{2+} + Cl^- \leftrightarrow Zn(Cl)^+$	0.46
$NH_4^+ + OH^- \leftrightarrow NH_3 + H_2O$	4.39
$Zn^{2+} + 2OH^- \leftrightarrow ZnO(s) + H_2O$	15.52

(b)

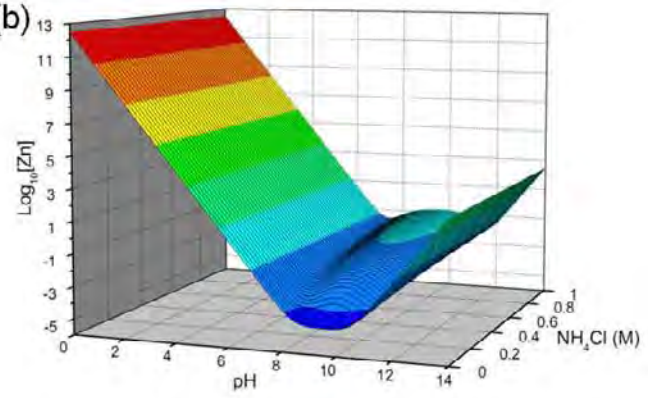

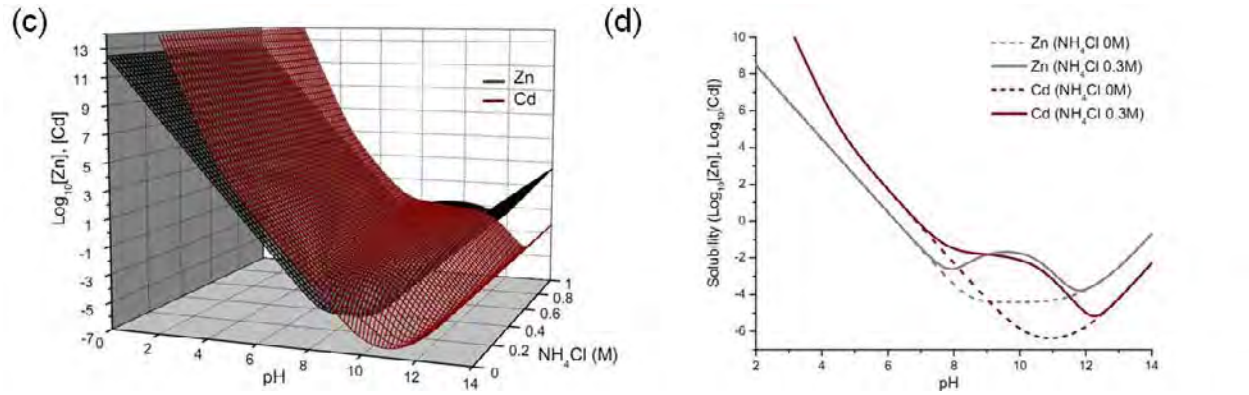

Fig. S2. **(a)** The possible chemical reactions in the ZnO nanowire bath solution and their reaction constants, and **(b)** the solubility plot calculated from the constants vs. pH (x-axis) and NH_4Cl concentration (y-axis). **(c)** Superimposed solubility plots of Zn (black) and Cd (red) calculated from the reaction constants. **(d)** Solubility plots of Zn and Cd with two different NH_4Cl concentrations (0 M, 0.3 M).

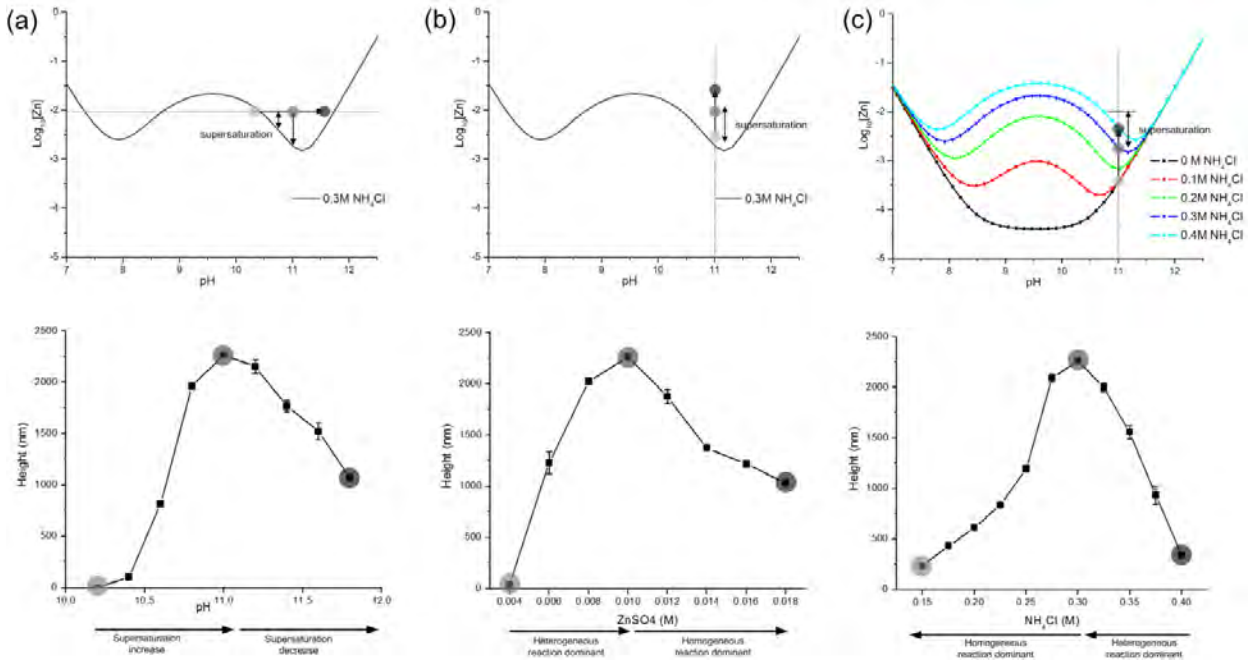

Fig. S3. (Top) Theoretical solubility plot and supersaturation amount (↕) and (Bottom) nanowire height as measured by cross-sectional SEM, with respect to **(a)** pH, **(b)** $ZnSO_4$ concentration, and **(c)** NH_4Cl concentration. Other parameters were kept fixed with a reference condition of: $[ZnSO_4]$ = 0.01 M, $[NH_4Cl]$ = 0.3M, pH = 11, 60°C, 100 mL solution volume, 6 hrs.

Calculated solubility plots and the SEM-measured growth rates under various synthesis conditions are shown in Figure S3. The solubility plot was a good indicator of real supersaturation levels. Based on the experimental results, we observed that supersaturation was the driving force for the phase change from liquid to solid, forming nanowires by heterogeneous nucleation and growth. At lower

DOI: 10.1038/NMAT3069

supersaturation, growth tends to be proportional to supersaturation degree as expected (Fig. S3a). However, less growth (defined as height of the nanostructure along the c-axis) was observed above a critical supersaturation ($[Zn^{2+}]$ > 10mM, Fig. S3b), because of competition from homogeneous nucleants in bulk solution that consume reagents. Between 10mM < $[Zn^{2+}]$ < 20mM, the solution color changed from transparent to turbid, indicating high levels of homogenous reactions (as shown in Fig. S1). Other parametric studies showed similar results with respect to $[NH_4Cl]$ (Fig. S3c), indicating that supersaturation is a key factor for estimating nanowire growth rate.

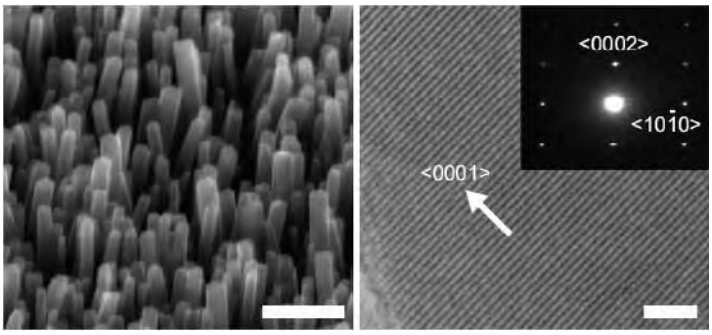

Fig. S4. (left) Scanning and (right) transmission electron micrographs of zinc oxide nanowires grown under the typical conditions (10 mM zinc sulfate, 0.3 M ammonium chloride, pH = 11, 60°C). The nanowires were single-crystalline, as evident by the x-ray diffraction pattern (right inset). Scale bar = 500 nm (left), 2 nm (right).

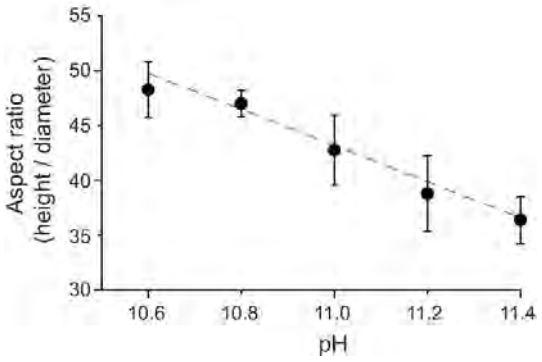

Fig. S5. Rational tuning of ZnO NW aspect ratio by altering solution pH to modulate the relative distribution of positively and negatively charged complex ions and the resultant face-selective adsorption and growth. Error bars represent one standard deviation.

Initial findings in pH-dependent morphological control studies (without the use of ancillary metal sulfates; Supplementary Fig. S5) were consistent with selective adsorption of reactive charged zinc complexes to the face of opposite measured charge, based on the thermodynamic calculations and measured surface charges via AFM (negative and positive for the (0002) and (10$\bar{1}$0) planes, respectively at pH = 11; Supplementary Fig. S6 and S7). Conditions that increase the local concentration of positively charged zinc ions at the negative (0002) surface (such as lower pH) lead to higher aspect ratio structures, and vice versa for negatively charged zinc complexes at the (10$\bar{1}$0) sidewalls. It is important to note that in this zinc-only case, there is little barrier to incorporation into the crystal. These findings are consistent with the literature[4-5].

III. ZnO surface potential for different crystalline faces

To evaluate whether electrostatic competition is a valid explanation for the experimental results, surface potentials of the (0002) plane and (10$\bar{1}$0) were analyzed by force-distance measurements made by atomic force microscopy. Au-coated AFM tips were functionalized with mercaptoundecanoic acid (in ethanol) [6] to ensure a negatively charged tip above pH 6.5 from a deprotonated carboxylate.

Figure S6 shows force-distance measurements with single crystalline surfaces of the (0002) Zn-terminated plane and the (10$\bar{1}$0) plane during approach to the surface. The (0002) plane showed an electrostatically repulsive long range force, indicating the surface is negatively charged below pH 11. This repulsive force and negative potential of the (0002) plane pH >11 agrees with previously reported findings [7]. The (10$\bar{1}$0) plane exhibited only an attractive force at pH 11, indicating the surface is positively charged. This data supports the assumption of a negatively charged (0002) and positively charged (10$\bar{1}$0) plane, that would have differential electrostatic interactions with charged species.

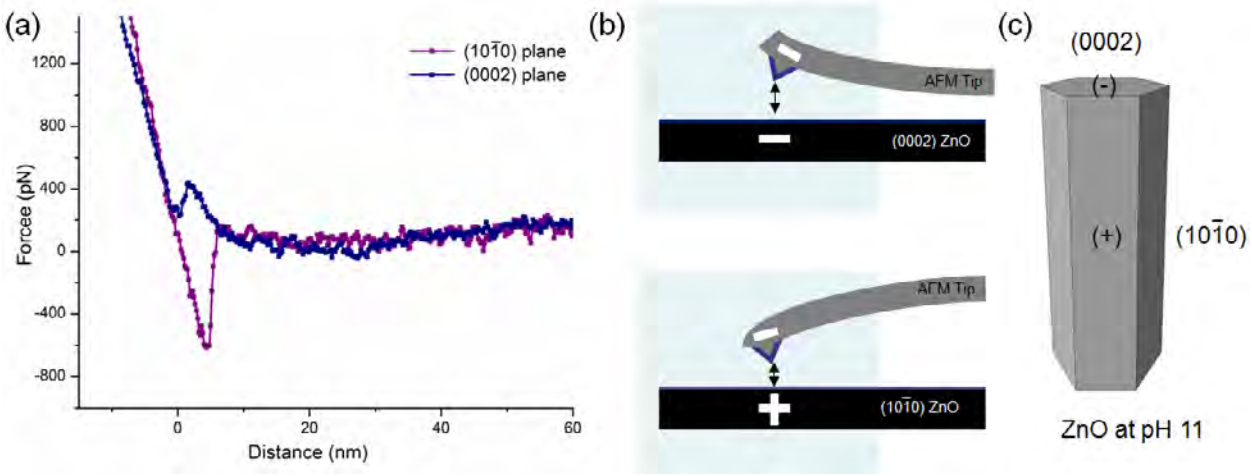

Fig. S6. (a) Force-Distance measurements (during tip-approach to the surface) of single crystalline (0002) and (10$\bar{1}$0) planes of ZnO at pH = 11, taken with carboxylate functionalized AFM tips. **(b)** Schematic of AFM tip-deflection by the two different planes at pH = 11, induced by electrostatic interactions between the charged surfaces. **(c)** Expected surface polarity of ZnO NWs under the experimental conditions.

The AFM experiments were not performed with solutions of the same chemical composition as the syntheses because the precipitation of species from a supersaturated solution would greatly confound the experiment and data interpretation. Thus, to further support the surface potential differences between planes, x-ray photoelectron spectroscopy (XPS) was performed.

XPS spectra of 3d photoelectron peaks and MMV Auger peaks of monolayer deposited Pd are shown in Figure S7. Auger peaks from the Pd signal on all three crystalline surfaces are identical. However, the photoelectron peaks of binding energies showed a difference of 0.25 eV between different crystal surfaces. The photoelectron peak of Pd on the (10$\bar{1}$0) surface had the lowest binding energy,

DOI: 10.1038/NMAT3069

while the peak on the $(11\bar{2}0)$ and (0002) surfaces were at 0.125 and 0.25 eV higher energies, respectively. Both modified auger parameter (MAP) and calculated cation density are shown in table S1. The surface with higher cation density has a lower MAP value. The correlation between MAP and surface charge can be explained by a classic electrostatic model that others reported for sapphire and titanium oxide crystals [8-9]. The binding energy of electrons from a Pd monolayer would increase with increasing net positive atomic charges at the crystalline interface. Therefore, the surface with higher binding energy will be more polarized at the solution interface, leading to stronger interactions with hydroxyl groups in solution, and thus require more aqueous protons to reach the isoelectric point (i.e. flip the surface charge from negative to positive). As a result, the surface plane with higher binding energy would have a lower isoelectric point (IEP). From the binding energy values measured, the $(10\bar{1}0)$ plane would have the highest IEP, followed by the $(11\bar{2}0)$ and (0002) planes. Since the (0002) surface has the highest binding energy, it would be more negatively charged compared than the $(10\bar{1}0)$ surface. This XPS data agrees with AFM data that suggests the (0002) surface is negatively charged at pH 11, but the $(10\bar{1}0)$ surface is still positively charged.

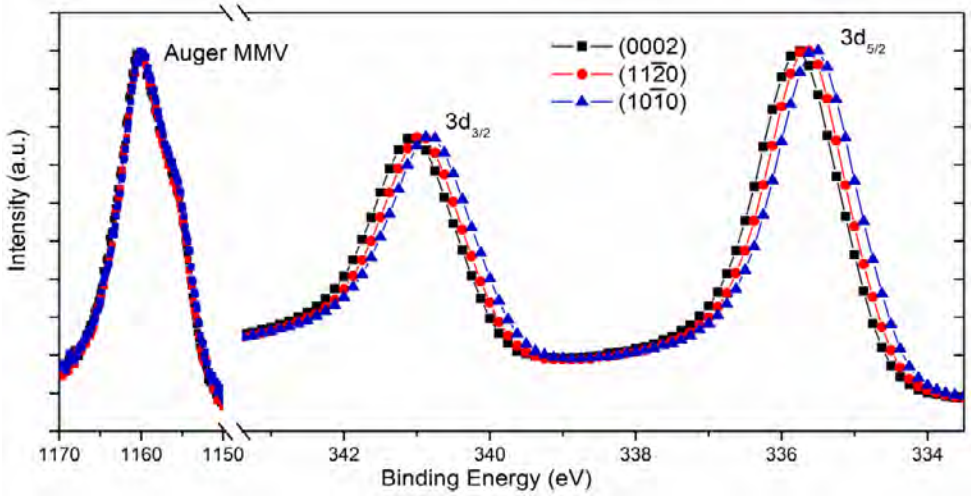

Fig. S7. XPS data of Auger MMV peak and photoelectron ($3d_{3/2}$ and $3d_{5/2}$) peaks of an atomic monolayer of palladium deposited on three different ZnO crystal surfaces. Differences in binding energies indicate differences in the extents to which electrons from Pd are bound to surface sites on their corresponding wurtzite ZnO substrates.

Orientation	M.A.P.	Cation density (per nm^2)
(0002) Zn terminated	824.375	10.9
$(11\bar{2}0)$	824.500	6.8
$(10\bar{1}0)$	824.625	5.9

Table S1. Modified Auger Parameters (MAP, difference between Auger and photoelectron peaks, where Auger peaks are of higher value) and cation density of ZnO crystals. Lower MAP corresponds to higher binding energies.

IV. Complex charge distribution for different cation species

To test whether face-specific electrostatic competition from non-zinc complex cations is generalizable beyond the addition of cadmium and aluminum ions, similar charged ion complex distributions were calculated for many other metal sulfates (Fig. S8). Note that in all cases, the presence of ancillary ions barely changes the distribution of zinc complex ions (< ±2%), which are typically ~80% positively charged under the growth conditions.

Like aluminum, indium and gallium species are primarily negatively charged and thus suppress the growth in the positively charged $(10\bar{1}0)$ plane, leading to higher spect ratio. Like cadmium, positively charged copper, magnesium, and calcium will suppress the growth in negatively charged (0002) plane, forming low aspect ratio plates as observed from the experiments. In terms of Zn complex ion distribution, there is a difference in Ca addition case (Fig. S8e) compared to other cation additions (Fig. S8a to S8d). It is because $Zn(OH)_2(aq)$ is mostly dominant at pH 8 ~ 12 region (Fig S8g), affected by high Ca reaction in the solution.

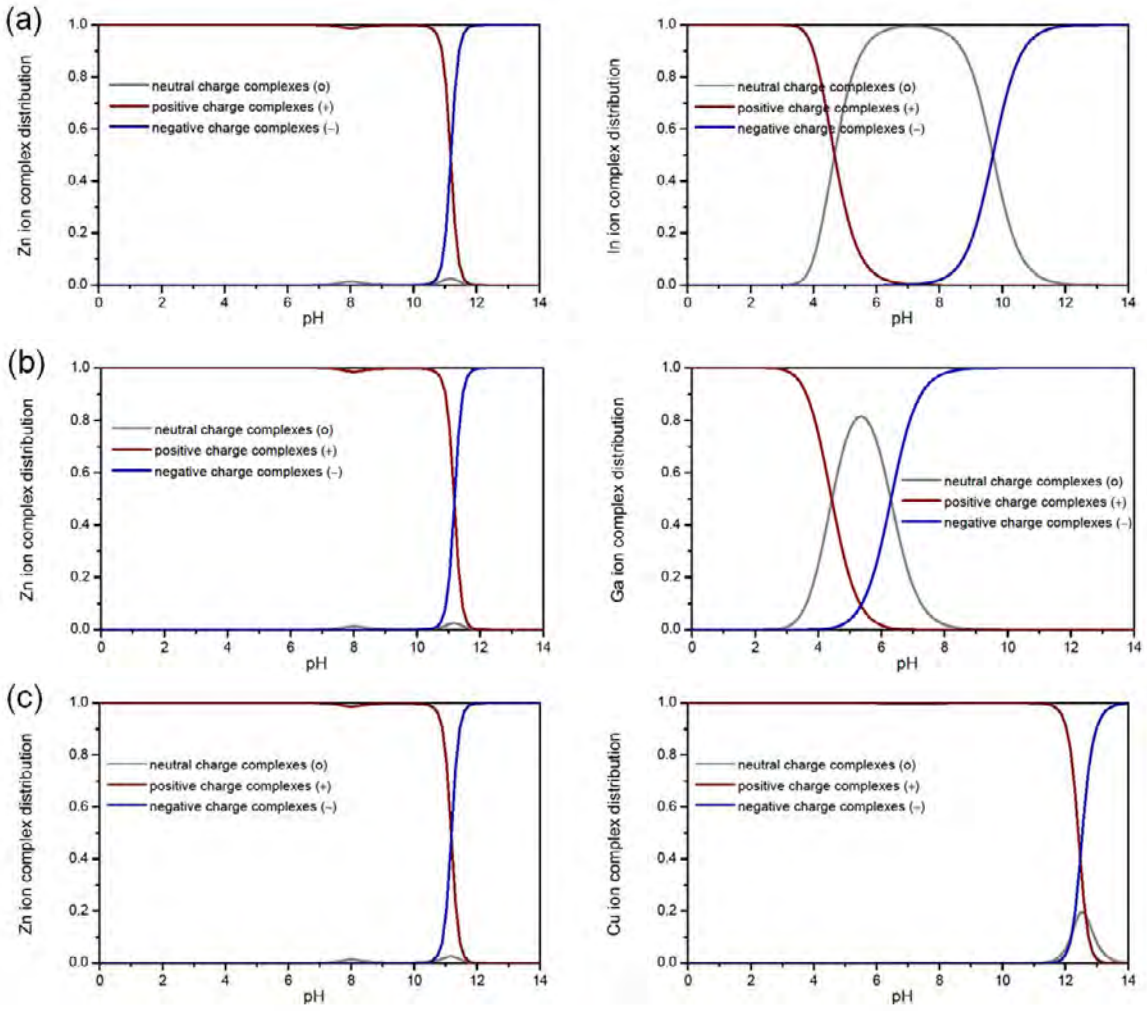

DOI: 10.1038/NMAT3069

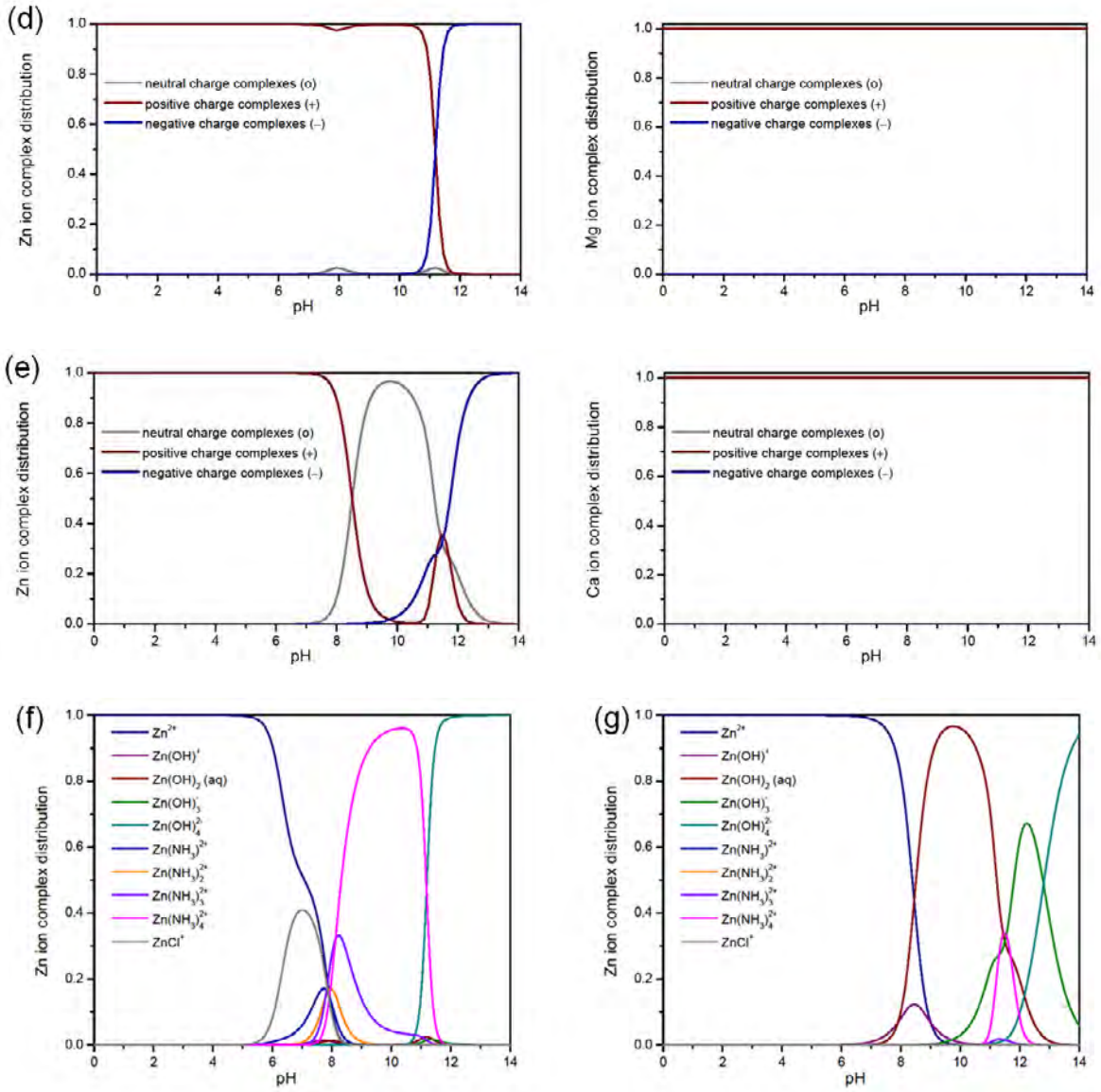

Fig. S8. (a) to (e) Speciation plots or charged complex ion distributions of **(left)** zinc and **(right)** additional cations (with 0.3M NH_4Cl): **(a)** In, **(b)** Ga, **(c)** Cu, **(d)** Mg, and **(e)** Ca. (f) Unbinned Zn complex ion speciation plot in the presence of Cu (as an exemplar similar to the unbinned Zn plots in the presence of all other ions tested except for Ca). (g) Unbinned Zn complex ion speciation plot in the presence of Ca.

Predictive modeling of nanowire growth trends in hydrothermal synthesis is complicated by the use of complex charge species with unknown binding constants and lack of measurements of surface charges on the growth face. For example, the possibility of polydentate binding or metal ion sequestering is seldom considered during the addition of polymeric carboxylates, sulfonates, and amines. Under the concentration conditions here ($[NH_4Cl] >> [ZnSO_4]$), the role of the sulfate counter-ion was minimized, thus leaving zinc hydroxide- and zinc amine-complexes as primary reactive intermediates whose relative concentrations could be calculated from known constants. By limiting uncertainty in ligand-metal interactions via simplification of ligands (to sulfate and ammonium

counterions only), in conjunction with the experimental determination of the surface charge, we could correlate data with a thermodynamic model that confirmed that morphology can be rationally controlled by electrostatic face-selective growth inhibition.

It is also important to note that the reaction temperature can affect the distribution of charged species and their solubility. Current solubility and speciation plots are calculated with available reaction constants at standard (25°C) condition. At high temperature, though, reaction constants will change and affect the ion complex distribution[10]. Unfortunately, not all thermodynamic data (temperature dependent heat capacity, entropy, and enthalpy) were available for each cation species to calculate the temperature dependent reaction constants. We believe that future work on thermodynamic parameters of specific ion complexes would complement our analysis on electrostatic control of nanowire synthesis over a wide range of temperatures.

V. Characterization of ZnO nanostructures grown in the presence of non-zinc cations

In the case of suppression of lateral growth in the $(10\bar{1}0)$ direction by Al, In, or Ga, the obelisk or needle shape at top of the nanowire was generally observed. This needle structure is different from the prismatic or pyramidal structures of ZnO with facets $(10\bar{1}1)$ formed at a 60° angle with the (0002) plane [11-15]. In our case, multiple steps were observed (instead of flat tilted face that would be the $(10\bar{1}1)$ plane), comprised of stacked hexagonal structures resulting in an obelisk with an angle of 87±0.9 degrees. It indicates that the needle-shaped tips arise from multiple layers of hexagonal crystal structures with gradually decreasing surface area and stacked on top of one another in the direction of the c-axis (Figure S9e) [16-18]. Suppression of sidewall growth would result in such a step-like structure for kinetic reasons, if diffusion along the top surface is hindered or insufficient to reach the edge of nanostructure before new stacking layers are nucleated (Figure S9f). This mechanism has previously described crevice and hillock formation in ZnO single crystal growth, when the vertical growth rate far exceeds the lateral one to induce formation of sharp needle-like tips [19].

DOI: 10.1038/NMAT3069

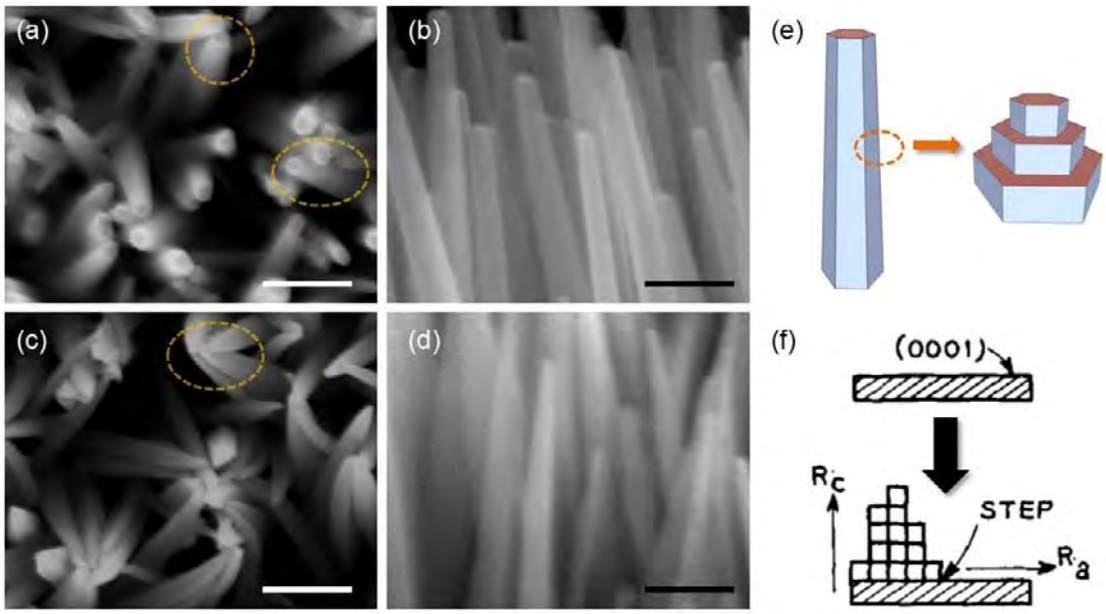

Fig. S9. Top and 90 degree tilted SEM images of nanowires grown in two different chemical solutions. (a,b) 0.0006M aluminum sulfate added to the standard reaction, (c,d) 0.002M aluminum sulfate added to the standard reaction. Scale bar = 200 nm. (e) Illustration of obelisk-formation from stacked planes of single-crystalline hexagonal structures. The mechanism is likely similar to (f) the introduction of crevices during growth of ZnO single crystals by step formation. Image taken from Laudise *et al*. [19].

Normalized XRD data for samples grown in the presence of different cations showed no change in crystalline orientation of ZnO nanowires (Fig. S10). All nanostructures showed a strong ZnO (0002) peak, indicating same vertical alignment of ZnO nanostructures. No other peaks of non-zinc metal or metal oxide phase were observed.

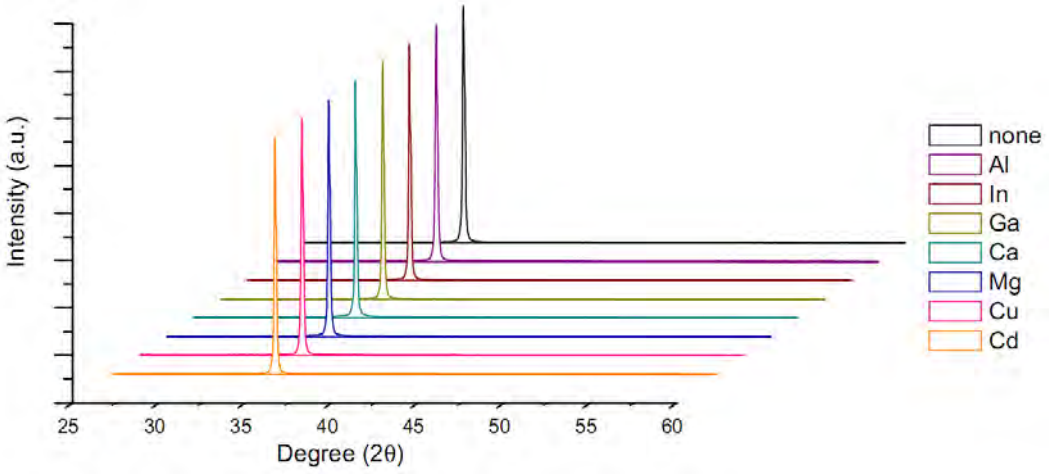

Fig. S10. X-ray diffraction pattern of hydrothermally synthesized ZnO nanowire grown in the presence of non-zinc cations (2 mM metal sulfates) on Si (100) substrates. The strong peaks indicate the (0002) ZnO peak. No other metal or metal oxide peaks were observed.

Photoluminescence (PL) data is shown in Figure S11. Every sample exhibited a distinctive band edge emission at ~ 378 nm, and defect related emission between 600 – 700 nm, possibly from oxygen interstitials, as is commonly observed with ZnO nanowires. No band edge peak shift was observed, indicating no optical band gap change via the potential formation of ternary phases from incorporated non-zinc cations (i.e. limited incorporation). However, differences in the relative amount of band edge emission vs. the defect state emission are observed, which may be attributable to incorporation. Defect emission could be largely eradicated by thermal annealing.

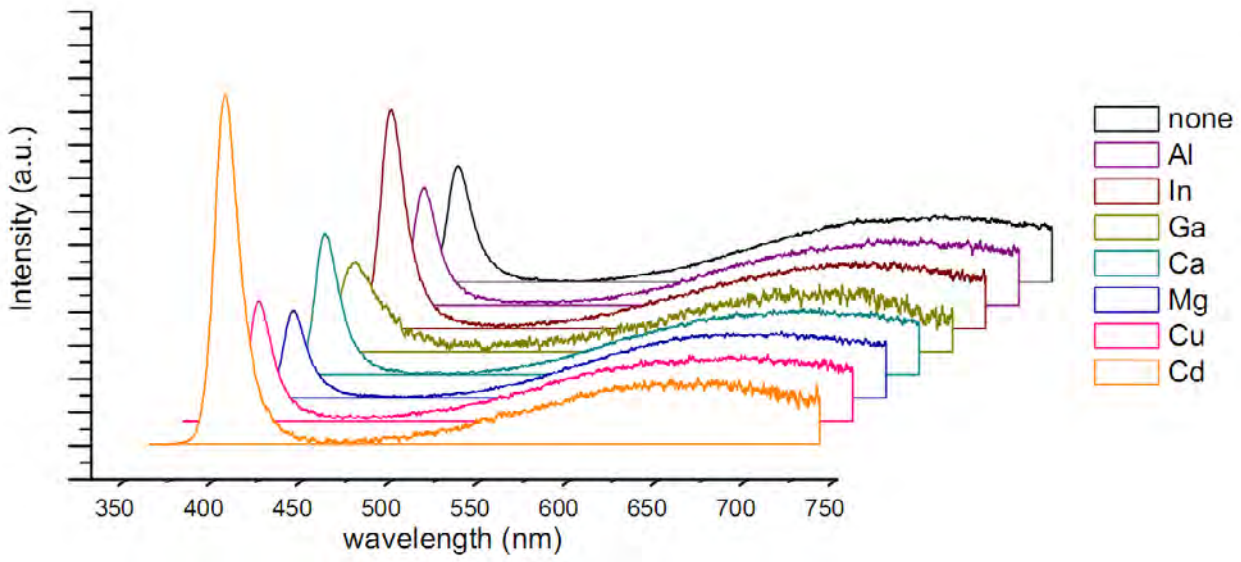

Fig. S11. Photoluminescence spectra of hydrothermally grown ZnO nanowires grown in the presence of various cation sulfates (2mM). The ultraviolet peak at 378 nm corresponds to the band edge emission of ZnO, and broad band defect emission between 600 - 700 nm were observed, as is commonly the case with unannealed ZnO nanostructures. No peak shift of band edge emission was observed.

VI. Thermodynamics of cation incorporation during synthesis

The maximum solubility is defined by a total free energy minimum. Assuming the system is a regular solid solution, and the non-zinc cation's corresponding metal (A) oxide has a limited solubility for Zn, then the solubility of species A in ZnO at a specific temperature is given as follows[20]

$$X_{A_{Zn}} = \exp\left(\frac{\Delta S}{k}\right) exp\left(-\frac{\Delta H}{kT}\right) \qquad \text{(eq. s1)}$$

where A_{Zn} is the A cation substituting for Zn, $X_{A_{Zn}}$ is the equilibrium solubility of A in ZnO, k is the Boltzmann constant, ΔS is the entropy change by cation substitution, ΔH is the formation enthalpy (energy required to substitute Zn with A). Note that "A" cation denoted here is by formalism, and is not limited to "A-type" cations as defined in this paper.

DOI: 10.1038/NMAT3069

ZnO has a wurtzite crystal structure, whereas CdO, CaO, and MgO have rock salt structures. To substitute Zn with A cations (such as Mg, Cd, Ca, or others), the system requires a high formation enthalpy (ΔH) because A_{Zn} would generate large localized stress to incorporate into a wurtzite structure. ΔH can be calculated from first principle lattice dynamic simulation[21-23]. In the case of MgO as an example with necessary constants available (and cited here), the energy required to change from rock salt structure to wurtzite is ~0.29 eV/formula unit[21], with similar values for CdO and CaO.

With respect to entropy, three different terms are involved: electronic entropy, vibration entropy, and configuration entropy. The electronic entropy contribution is small due to the wide band gap, and vibration entropy does not have a large contribution[21]. The configuration entropy of simple mixing of x (mol%) can be expressed as:

$$\Delta S_{conf} = -k[xlnx + (1-x)\ln(1-x)] \qquad \text{(eq. s2)}$$

The value above will be in the range of 0 to ~1.39k. Given that the maximum thermodynamic solubility of Mg in ZnO is ~3% [24], we can assume $\exp(\Delta S/k)$ to be ~2 as an approximation, although the value can vary within a range.

Based on equation s1, the calculated temperature dependent solubility of A with the values determined above (0.29eV/atom; $\exp(\Delta S/k)$=2) is shown in Figure S12. Because of the high formation enthalpy, incorporation of A is energetically unfavorable at low temperatures. The calculated maximum solubility of A in ZnO under our experimental conditions (60°C, 333K) is $8.24\text{x}10^{-5}$. Because of this low solubility, the electrostatically adsorbed non-zinc complexes will mainly block the available crystal surface sites to inhibit Zn complex binding, but will not incorporate into the crystal (or as measurable in our hands). However, at high temperature, entropy overcomes the high formation enthalpy and the solubility of A in ZnO increases. For example, the solubility during a hydrothermal ZnO synthesis at temperature sufficient to enable slight doping[25-26] (300°C, 573K) would be $5.66\text{x}10^{-3}$, almost two orders of magnitude larger than the solubility under the low temperature conditions reported here (Fig. S12b). As a first approximation, our calculated estimates are in good agreement with reported measured percent incorporation by dopants into hydrothermally synthesized ZnO[27].

Similar thermodynamic calculations can be performed for the Zn solubility or incorporation into the foreign metal oxide structure, such as MgO or CdO (denoted as AO). In the case of ZnO inclusion into AO, the energy required to change ZnO from its wurtzite structure to rock salt structure is ~0.21 eV/formula unit[21]. Because the required energy is lower in this case vs. opposite case described above (i.e. AO conversion from rock salk to wurtzite requires ~0.29 eV/formula unit), the solubility of Zn in the rock salt structure AO would be higher than the solubility of A in the wurtzite structure ZnO, as shown in Figure S12(c) and (d). Thus, at high concentration of non-zinc metal sulfate or extremely long reaction times (see Section VII.A immediately below), one must keep attuned to the depletion of zinc species in the homogenously nucleating foreign oxide structures in bulk solution.

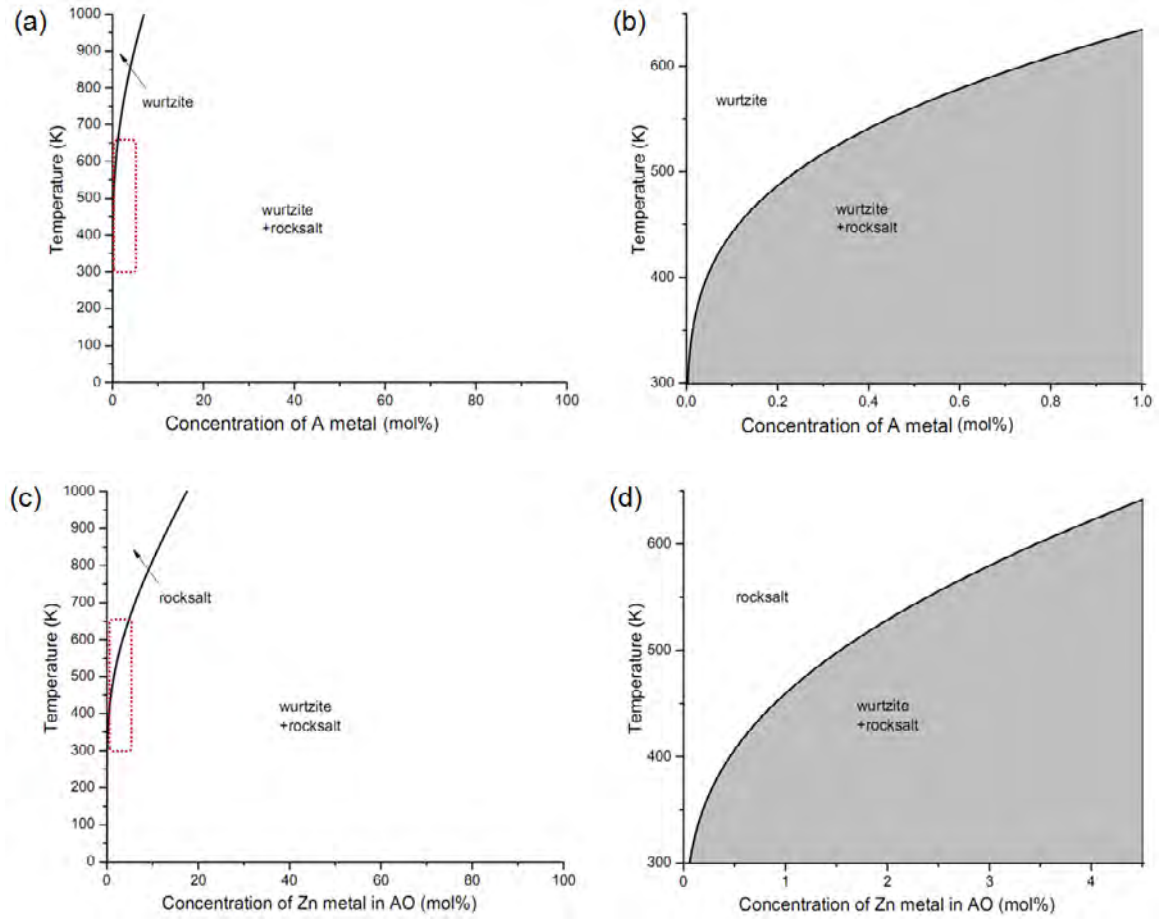

Fig. S12. (a) Temperature dependent solubility plot of rock salt structure foreign metal oxide into wurtzite structure ZnO, with formation energy of 0.29eV and $\exp(\Delta S/k)$ of 2 approximated based on MgO. (b) Solubility plot between 300K and 650K, corresponding to the red box in Figure S12a. (c) Temperature dependent solubility plot of wurtzite structure ZnO in AO with rock salt structure, with formation energy of 0.21eV and $\exp(\Delta S/k)$ of 2 approximated based on MgO. (d) Solubility plot between 300K and 650K, corresponding to the red box in Figure S12d.

VII. Contributions to morphology control by parameters beyond electrostatics

Many factors beyond electrostatics can influence hydrothermal synthesis, and are detailed below. However, our analyses suggest that electrostatic interaction between complex ion and growing surface is the dominant mechanism of morphology control at alkaline pH.

VII.A. Time dependent effects on ZnO growth – pH and reagent depletion

The time dependent ZnO height, diameter, and aspect ratio are shown in Figure S13. In the absence of a modifier (Figure S13a), rapid growth was observed after the first ~4 hours (initial stage), and then a consistent growth rate was observed for up to 20 hours (growth stage). No apparent asymptote of growth was observed. The aspect ratio of the nanowires was consistent throughout the experiment varying by ± 1.5% over the 20 hour period, measured in 4 hour intervals. This indicates that

DOI: 10.1038/NMAT3069

the growth is mostly limited by the kinetic diffusion of ions to the ZnO facets. Over this 20-hour period, the solution pH was changed very modestly from 11 to 10.8; it is not anticipated to have a major impact here, but must be kept attuned to over extremely long reaction durations.

However, when synthesized in the presence of Cd ions (Fig. S13c), the time-dependent aspect ratio was less consistent, steadily decreasing over the 20 hour period (albeit by a modest 20% total). The depletion of available Zn complex ions would lead to an increase in relative Cd concentration, the latter of which is not incorporated into the growing crystal and thus depletes less. This relative increase in Cd concentration ratio would lead to even lower aspect ratio platelets, as observed experimentally. Thus, depletion of reagents must be kept attuned to over long reactions, when in the presence of modifiers.

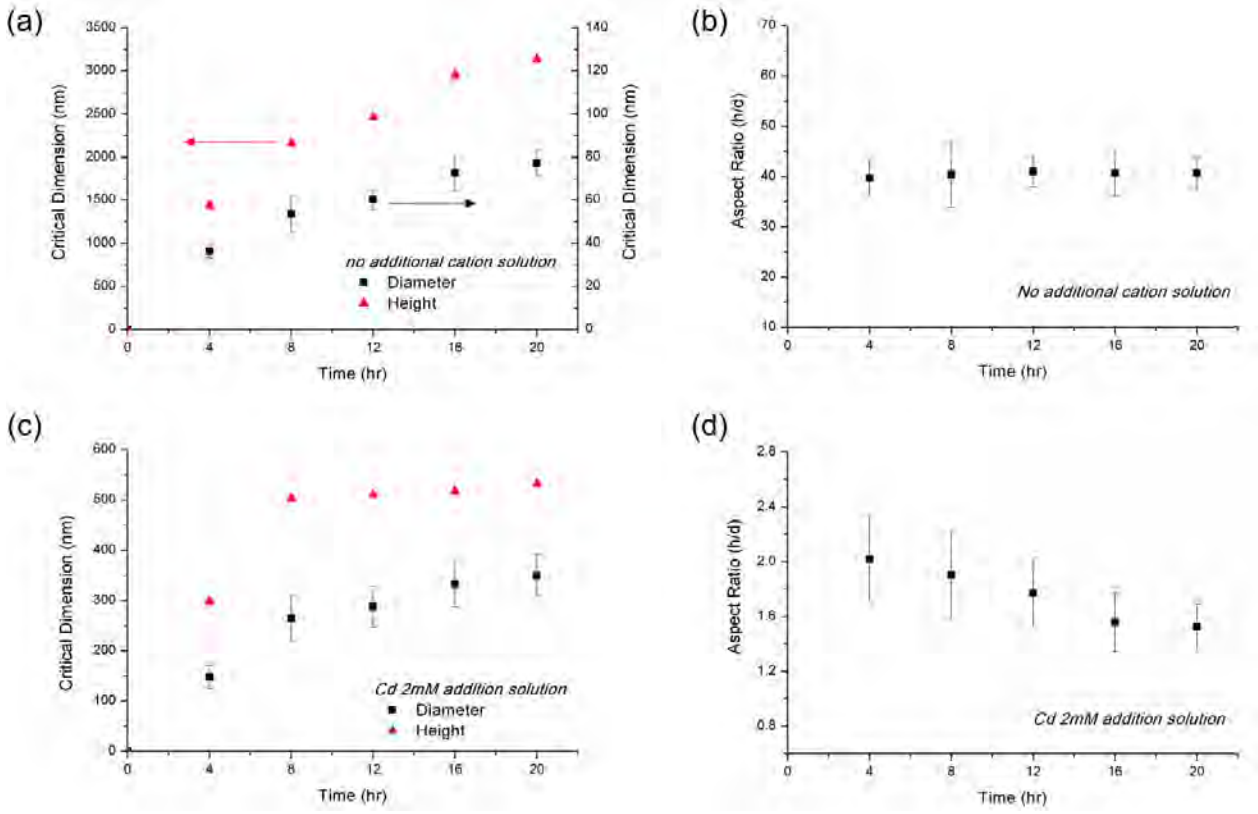

Fig. S13. Time dependent measurement of nanowire height and diameter grown in the absence of non-zinc divalent cations (a) and calculated aspect ratio (b). Time dependent measurement of nanowire height and diameter grown in the presence of 2mM Cd cations (c) and calculated aspect ratio (d). Error bars represent one standard deviation. Arrows in (a) are to guide the eye to the appropriate y-axis label.

VII.B. Contributions by interactions with anionic counter-ions and chemisorption

The role of counter-ion interaction is anticipated to be negligible under the alkaline and chemical composition conditions reported here. While sulfates selectively adsorb at the polar c-faces which can lead to low aspect ratio platelets at low pH[28], c-axis-preferring growth is observed here, thus indicating that sulfate adsorption does not play a major role in the crystal growth inhibition. The high concentration

of chloride can impact the speciation plot at neutral pH and by electrochemical approaches[29-30], but have negligible impact on the distribution of species under alkaline conditions, as determined by comparing speciation plots with and without chloride factored into the classical thermodynamic model.

Chemisorption of organic ligands can play a role in crystal growth inhibition (as summarized in Govender *et al.*[28]), particularly with carboxylate ions at the ZnO interface; Tian *et al.*[31] leveraged this interaction to alter ZnO morphology by introducing citrate at neutral pH, and similar use of polyethylenimine to alter morphology is well documented[32]. However, the addition of such modifiers did not have an effect under the alkaline reaction conditions here.

Chemisorption of metal complex-ions can have other potential mechanisms of action, such altering the point of zero charge values, but not under the alkaline synthesis conditions here in any dramatic fashion (based on data from reference[33]); However, one must keep attuned to such alterations near neutral pH. Chemisorbed metal complex-ions may also act as nucleation points[34-35], but no such effects were observed, presumably because an existing seed layer is already present to nucleate heterogenous growth. The polarizability of the complex ions is anticipated to be negligible as well; of the reactive zinc species only ZnOH and $ZnNH_3$ are polarizable, but their relative concentrations are insignificant (~10^{-5}).

VIII. Electrical and optical properties of nanowire optoelectronic devices

VIII.A. *Field emission properties of ZnO nanowires*

Electron emission under an applied field can be described by Fowler-Nordheim (FN) equations,

$$J = A\frac{E^2}{\varphi}\exp\left(-\frac{B\varphi^{3/2}}{E}\right) \qquad \text{(eq. s3)}$$

where J is the current density (A/cm^2), E is the electric field (V/um), A and B are constants (A = 1.56 x 10^{-10} A·eV/V^2, B = 6.83 x 10^3 eV$^{-3/2}$ V/um), and φ is the work function of ZnO (5.3 eV) [36-38].

Local electric field can be described as,

$$E = \beta V/d \qquad \text{(eq. s4)}$$

where β is the field enhancement factor, V is the applied voltage, and d is the spacing between electrode and nanowire tip.

Arranging equation (eq. s3) with (eq. s4) gives the following FN plot,

$$\ln\left(\frac{I}{V^2}\right) = \ln\left(\frac{A\beta^2}{d^2\varphi}\right) - \frac{B\varphi^{3/2}d}{\beta V} \qquad \text{(eq. s5)}$$

The slope of the FN plot (k) is determined by the field enhancement factor (β) and work function (φ).

DOI: 10.1038/NMAT3069

Field emission data with five different nanowire samples were plotted again with FN curve (**Fig. S14a**). From the slopes of FN curves, the field enhancement factor for each nanowire device was calculated (**Fig. S14b**).

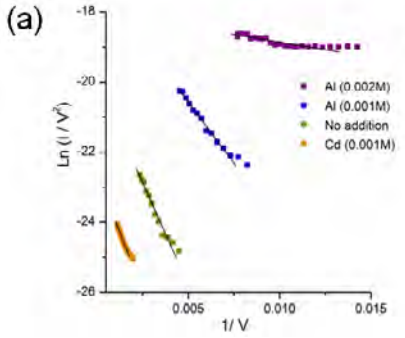

(b)

Nanowires	Slope of FN curves (k)	Field enhancement factor (β)
Al 0.002 M	-86.0	28246.6
Al 0.001 M	-489.6	4962.4
No addition	-1166.5	2082.9
Cd 0.001 M	-1363.6	1781.8
Cd 0.002 M	N/A	N/A

Fig. S14. (a) Fowler-Nordheim (FN) plots for ZnO nanowire of varying aspect ratio. **(b)** Slopes of FN curves and calculated field enhancement factors for the ZnO nanowires.

VIII.B. *Nanowire ACEL device*

Photoluminescence spectra of ZnS:Mn deposited on quartz substrates and electroluminescence spectra of ZnO nanowire-embedded ACEL devices are shown in Figure S15. The yellow/orange PL originates from the energy release of manganese electrons from the photoexcited states to the ground states. The EL maximum peak was almost identical to the Gaussian fitted PL maximum of 592 nm, indicating that the EL originates from energy transfer from the excited states to the ground states of manganese electrons, as opposed to from the ZnO. It should be noted, that the electron excitation mechanism is different from photoexcitation; in an ACEL device, the high electric field across the phosphor creates accelerated electrons in the layer or tunneling electrons from the dielectric layer, that impact the ground electrons of Mn. There was no difference in the EL spectra with and without nanowires (image not shown), indicating that ZnO nanowires serve only as a field enhancing layer, not an active light emitting layer.

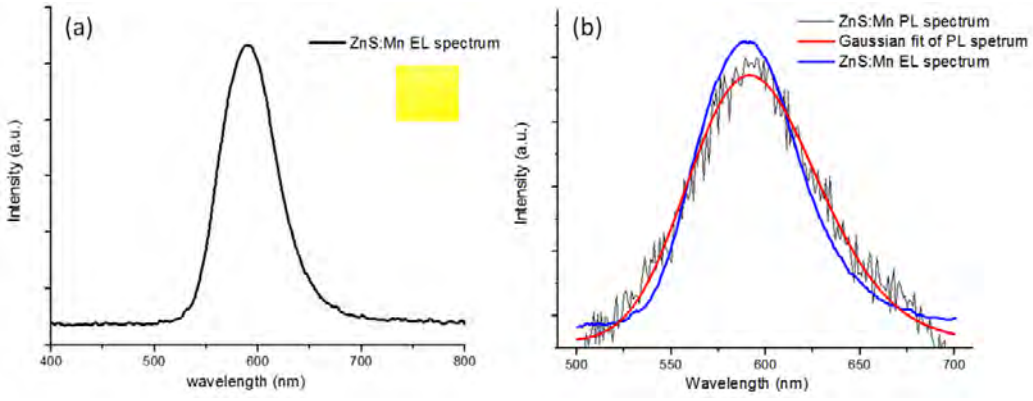

Figure S15. (a) ZnS:Mn electroluminescence spectra measured for a nanowire-embedded ACEL device running at 300 V and 5 kHz. **Inset:** color image captured from the device. **(b)** ZnS:Mn phosphor PL and device EL spectra comparison.

Depending on the ZnO nanostructures embedded in ACEL device, the maximum efficiency changed drastically (**Table S2**). High aspect ratio devices (Al 0.002M) showed greater than a 10-fold increase in maximum efficiency (0.065 lm/W) compared to ACEL devices without nanowires (0.006 lm/W). Further optimization, particularly with respect to phosphor composition, is expected to enhance absolute performance.

sample	Turn on voltage (V at 1cd/m2)	luminance (cd/m^2)	Max Luminous efficiency (lm/W)	Notes
Al 0.002 M	~ 160	131	0.065	High aspect ratio nanowires embedded
No addition	~170	54.7	0.009	Nanowires embedded
Cd 0.002M	~230	30.2	0.0064	Nanoplates embedded
Control (no NW)	~ 300	22.7	0.006	N/A
$\{(Y_2O_3)_{1-x}-(GeO_2)_x\}$:Mn / $BaTiO_3$[a]	< 100	7,700, 724	1.0, 9.5	New phosphor, anneal at 1020C
ZnS:Mn / Y_2O_3[b]	~ 200	1,800	1.2	Anneal at E-field , oxygen glow discharge
ZnS:Mn / $BaTiO_3$ sheet[c]	~ 20	6,300	11	ZnS:Mn by MOCVD
Cold Cathode Fluorescent light[d] (LCD backlight)	N/A (120~1500 at run)	32,000	60 ~ 70	In production
CNT FED[e]	N/A (1kV at run)	10,000	31	Printed CNT for BLU
LED[f]	0 ~ 2	50 ~ 110	208	New record for white LED
OLED[g]	2.5 ~ 3	1,000 ~ 10,000	90	Pattern surface for high extraction efficiency

Table S2. Comparison of ACEL device performances, including other reported technologies. [a]Ref [39]. [b]Ref [40]. [c]Ref [41]. [d]Ref [42]. [e]Ref [43]. [f]Ref [44]. [g]Ref [45].

VIII.C. *Microfluidic metal-insulator-semiconductor (M-I-S) device*

The schematized protocol for microfluidic nanowire synthesis is shown in Figure S16. After spin coating or RF sputtering a thin ZnO seed layer on a pre-cleaned substrate, molded polydimethylsiloxane (PDMS) fluidic channels were attached to the substrate either by mechanically pressurized contact or plasma bonding. Supersaturated solutions were flown through each channel, and surface-confined nanowires were synthesized at temperatures from 40-80 °C, with temperature control achieved via a Peltier stage.

Low temperature aqueous synthesis can be utilized in a microfluidic environment as a parallel screening tool for further parametric study of the growth system, and also for the formation of *in-situ* fabricated devices. Nanowires of different morphology were synthesized in individual channels of a microfluidic manifold (Figure S17), using solutions of identical composition to those used in bulk syntheses; the resultant aspect ratios of the nanowires were approximately the same.

The current-voltage (I-V) trace of an *in-situ* fabricated microfluidic M-I-S LED is shown in Figure S18, demonstrating a rectifying behavior as would be expected of a diode.

DOI: 10.1038/NMAT3069

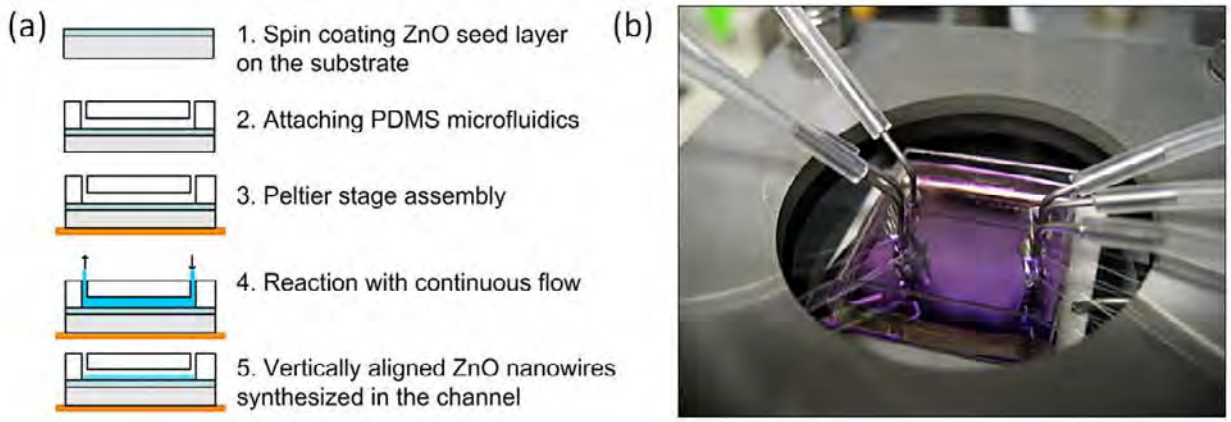

Fig. S16. Schematic diagram of microfluidic ZnO nanowire synthesis (a) and device with three parallel channels (b).

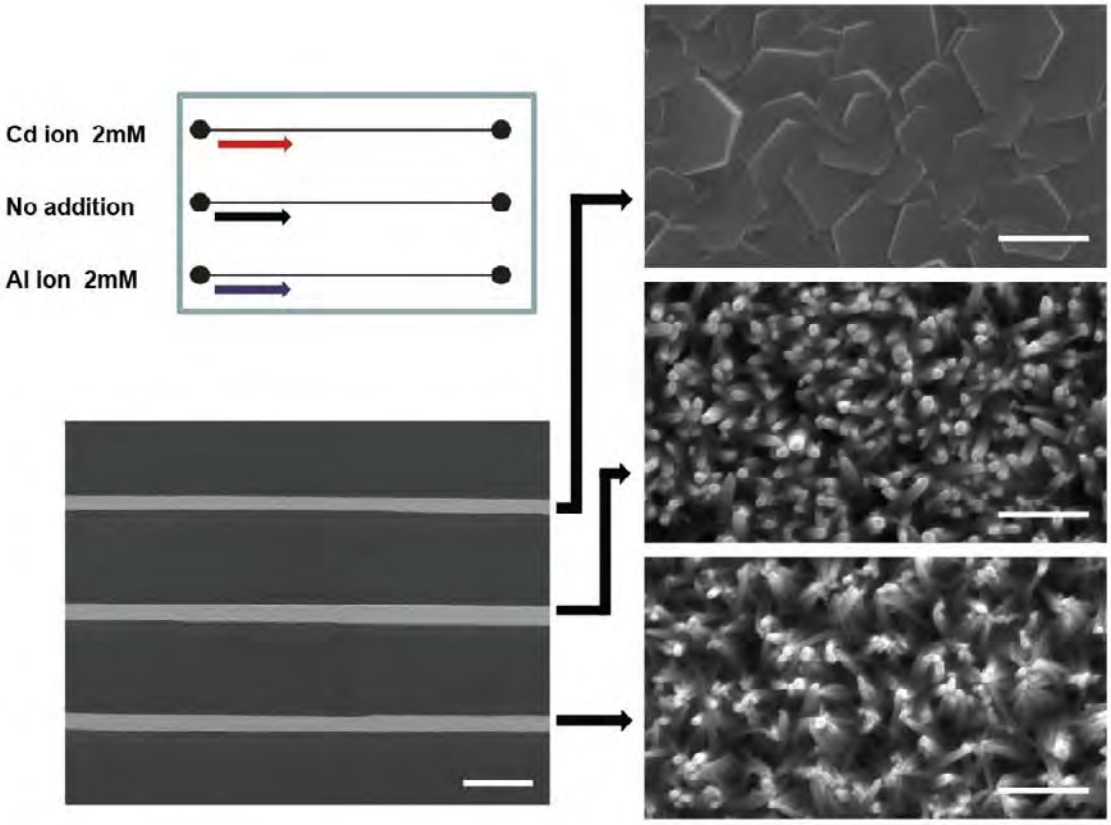

Fig. S17. Schematic of microfluidic channels for parallel screening of nanowire synthesis conditions (upper left), and SEM (bottom left) of different ZnO nanostructures simultaneously grown on a single substrate (after PDMS manifold detachment). High resolution SEM images (right) show similar morphology changes induced in non-microfluidic synthesis via electrostatic competition from non-zinc cations. Scale Bar = 250 um (left), 500 nm (right).

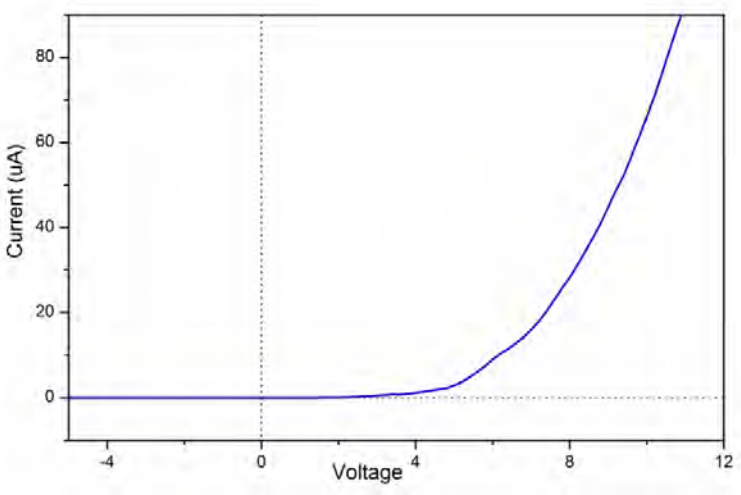

Fig. S18. Current-Voltage characteristic of the M-I-S LED formed and packaged within a microfluidic manifold. The nonlinear IV trace demonstrates diode rectification.

REFERENCES

1 Prakash, M. & Gershenfeld, N. Microfluidic Bubble Logic. *Science* **315**, 832-835 (2007).

2 Kong, D. S., Carr, P. A., Chen, L., Zhang, S. & Jacobson, J. M. Parallel gene synthesis in a microfluidic device. *Nucleic Acids Research* **35**, e61 (2007).

3 Siegel, A. C., Bruzewicz, D. A., Weibel, D. B. & Whitesides, G. M. Microsolidics: Fabrication of Three-Dimensional Metallic Microstructures in Poly(dimethylsiloxane). *Advanced Materials* **19**, 727-733 (2007).

4 Richardson, J. J. & Lange, F. F. Controlling Low Temperature Aqueous Synthesis of ZnO. 1. Thermodynamic Analysis. *Crystal Growth & Design* **9**, 2570-2575 (2009).

5 Belghiti, H. E., Pauporté, T. & Lincot, D. Mechanistic study of ZnO nanorod array electrodeposition. *physica status solidi (a)* **205**, 2360-2364 (2008).

6 Schweiss, R., Welzel, P. B., Werner, C. & Knoll, W. Dissociation of Surface Functional Groups and Preferential Adsorption of Ions on Self-Assembled Monolayers Assessed by Streaming Potential and Streaming Current Measurements. *Langmuir* **17**, 4304-4311 (2001).

7 Valtiner, M., Borodin, S. & Grundmeier, G. Stabilization and Acidic Dissolution Mechanism of Single-Crystalline ZnO(0001) Surfaces in Electrolytes Studied by In-Situ AFM Imaging and Ex-Situ LEED. *Langmuir* **24**, 5350-5358 (2008).

8 Kershner, R. J., Bullard, J. W. & Cima, M. J. Zeta potential orientation dependence of sapphire substrates. *Langmuir* **20**, 4101-4108 (2004).

9 Bullard, J. W. & Cima, M. J. Orientation dependence of the isoelectric point of TiO_2 (rutile) surfaces. *Langmuir* **22**, 10264-10271 (2006).

10 Goux, A., Pauporte, T., Chivot, J. & Lincot, D. Temperature effects on ZnO electrodeposition. *Electrochimica Acta* **50**, 2239-2248 (2005).

11 Pradhan, D., Kumar, M., Ando, Y. & Leung, K. T. Fabrication of ZnO Nanospikes and Nanopillars on ITO Glass by Templateless Seed-Layer-Free Electrodeposition and Their Field-Emission Properties. *ACS Applied Materials & Interfaces* **1**, 789-796 (2009).

12 Li, W.-J., Shi, E.-W., Zhong, W.-Z. & Yin, Z.-W. Growth mechanism and growth habit of oxide crystals. *Journal of Crystal Growth* **203**, 186-196 (1999).

13 Zhang, Z. & Mu, J. Hydrothermal synthesis of ZnO nanobundles controlled by PEO-PPO-PEO block copolymers. *Journal of Colloid and Interface Science* **307**, 79-82 (2007).

14 Song, T. *et al.* Surface Polarity and Shape-Controlled Synthesis of ZnO Nanostructures on GaN Thin Films Based on Catalyst-Free Metalorganic Vapor Phase Epitaxy. *Advanced Materials* **20**, 4464-4469 (2008).

15 Mu, G., Gudavarthy, R. V., Kulp, E. A. & Switzer, J. A. Tilted Epitaxial ZnO Nanospears on Si(001) by Chemical Bath Deposition. *Chemistry of Materials* **21**, 3960-3964 (2009).

16 Wang, Z., Qian, X.-f., Yin, J. & Zhu, Z.-k. Aqueous solution fabrication of large-scale arrayed obelisk-like zinc oxide nanorods with high efficiency. *Journal of Solid State Chemistry* **177**, 2144-2149 (2004).

17 Li, P., Liu, H., Xu, F.-x. & Wei, Y. Controllable growth of ZnO nanowhiskers by a simple solution route. *Materials Chemistry and Physics* **112**, 393-397 (2008).

18 Li, P., Wei, Y., Liu, H. & Wang, X. A simple low-temperature growth of ZnO nanowhiskers directly from aqueous solution containing $Zn(OH)_4^{2-}$ ions. *Chemical Communications*, 2856-2857 (2004).

19 Laudise, R. A., Kolb, E. D. & Caporaso, A. J. Hydrothermal Growth of Large Sound Crystals of Zinc Oxide. *Journal of the American Ceramic Society* **47**, 9-12 (1964).

20 Porter, D. A. & Easterling, K. E. *Phase Transformation in Metals and Alloys*. 2 ed., CRC Press, United Kingdom (1992).

21 Seko, A., Oba, F., Kuwabara, A. & Tanaka, I. Pressure-induced phase transition in ZnO and ZnO-MgO pseudobinary system: A first-principles lattice dynamics study. *Physical Review B* **72**, 024107 (2005).

22 Maznichenko, I. V. *et al.* Structural phase transitions and fundamental band gaps of $Mg_xZn_{1-x}O$ alloys from first principles. *Physical Review B* **80**, 144101 (2009).

23 Fan, X. F. & et al. A first-principle analysis on the phase stabilities, chemical bonds and band gaps of wurtzite structure $A_xZn_{1-x}O$ alloys (A = Ca, Cd, Mg). *Journal of Physics: Condensed Matter* **20**, 235221 (2008).

24 Sarver, J. F., Katnack, F. L. & Hummel, F. A. Phase Equilibria and Manganese-Activated Fluorescence in the System $Zn_3(PO_4)_2$-Mg_3 $(PO_4)_2$. *Journal of the Electrochemical Society* **106**, 960-963 (1959).

25 Demianets, L. N. & Kostomarov, D. V. Mechanism of zinc oxide single crystal growth under hydrothermal conditions. *Annales de Chimie Science des Matériaux* **26**, 193-198.

26 Demianets, L. N., Kostomarov, D. V., Kuz'mina, I. P. & Pushko, S. V. Mechanism of growth of ZnO single crystals from hydrothermal alkali solutions. *Crystallography Reports* **47**, S86-S98 (2002).

27 Bai, S. N., Tsai, H. H. & Tseng, T. Y. Structural and optical properties of Al-doped ZnO nanowires synthesized by hydrothermal method. *Thin Solid Films* **516**, 155-158 (2007).

28 Govender, K., Boyle, D. S., Kenway, P. B. & O'Brien, P. Understanding the factors that govern the deposition and morphology of thin films of ZnO from aqueous solution. *Journal of Materials Chemistry* **14**, 2575-2591 (2004).

29 Elias, J., Tena-Zaera, R. & Levy-Clement, C. Effect of the Chemical Nature of the Anions on the Electrodeposition of ZnO Nanowire Arrays. *The Journal of Physical Chemistry C* **112**, 5736-5741 (2008).

30 Tena-Zaera, R., Elias, J., Wang, G. & Lévy-Clément, C. Role of Chloride Ions on Electrochemical Deposition of ZnO Nanowire Arrays from O_2 Reduction. *The Journal of Physical Chemistry C* **111**, 16706-16711 (2007).

31 Tian, Z. R. *et al.* Complex and oriented ZnO nanostructures. *Nat Mater* **2**, 821-826 (2003).

32 Law, M., Greene, L. E., Johnson, J. C., Saykally, R. & Yang, P. *Nat. Mater.* **4**, 455 (2005).

33 Degen, A. & Kosec, M. Effect of pH and impurities on the surface charge of zinc oxide in aqueous solution. *Journal of the European Ceramic Society* **20**, 667-673 (2000).

34 Kokotov, M. & Hodes, G. Reliable chemical bath deposition of ZnO films with controllable morphology from ethanolamine-based solutions using $KMnO_4$ substrate activation. *Journal of Materials Chemistry* **19**, 3847-3854 (2009).

35 Kokotov, M., Biller, A. & Hodes, G. Reproducible Chemical Bath Deposition of ZnO by a One-Step Method: The Importance of "Contaminants" in Nucleation. *Chemistry of Materials* **20**, 4542-4544 (2008).

36 Lee, C. J. *et al.* Field emission from well-aligned zinc oxide nanowires grown at low temperature. *Applied Physics Letters* **81**, 3648-3650 (2002).

37 Tseng, Y. K. *et al.* Characterization and field-emission properties of needle-like zinc oxide nanowires grown vertically on conductive zinc oxide films. *Advanced Functional Materials* **13**, 811-814 (2003).

38 Yang, Y. H., Wang, B., Xu, N. S. & Yang, G. W. Field emission of one-dimensional micro- and nanostructures of zinc oxide. *Applied Physics Letters* **89** (2006).

39 Minami, T., Kobayashi, Y., Miyata, T. & Suzuki, S. High-luminance thin-film electroluminescent devices using $((Y_2O_3)_{0.6}$-$(GeO_2)_{0.4})$: Mn phosphors. *Japanese Journal of Applied Physics Part 2-Letters* **41**, L577-L579 (2002).

40 Kutty, T. R. N. Effect of deposition conditions on the aging of a.c. thin film electroluminescent devices. *Thin Solid Films* **127**, 223-232 (1985).

41 Nanto, H., Minami, T., Murakami, S. & Takata, S. Low-voltage-driven ZnS-Mn thin film electroluminescent devices using insulating dielectric ceramic sheets. *Thin Solid Films* **164**, 363-367 (1988).

42 *http://worldoflcd.com/backlight_units_ccfl_tubes.htm*

43 Kim, Y. C. & Yoo, E. H. Printed carbon nanotube field emitters for backlight applications. *Japanese Journal of Applied Physics Part 2-Letters & Express Letters* **44**, L454-L456 (2005).

44 *http://www.cree.com/*

45 Reineke, S. *et al.* White organic light-emitting diodes with fluorescent tube efficiency. *Nature* **459**, 234-U116 (2009).